

# Study of customised high-efficient perovskite based mini-modules

Optimization of Laser scribing parameters

MSc Thesis Sustainable Energy Technology

Pavithran Kuppuswamy Saravanan

# Study of customised high-efficient perovskite based mini-modules Optimization of Laser scribing parameters

by

Pavithran Kuppuswamy Saravanan

Student Name	Student Number
Pavithran Kuppuswamy Saravanan	5276802

Supervisors: Dr.Ivan Gordon  
Daily Supervisor: Aranzazu Aguirre  
Institution: Delft University of Technology  
Place: Faculty of Engineering, Mathematics and Computer science, Delft  
Project Duration: November, 2021 - July, 2022

# Acknowledgements

I am proud to have accomplished one of my goals in the professional phase of my life. The knowledge and experience acquired in the past two years will hold me in good stead, and I am excited to bring more sustainable ideas to society. Thanks to TU Delft, the PVMD faculty, and the IMEC for the fantastic opportunity. Further, I want to thank my thesis supervisors, Dr.Ivan Gordon and Aranzazu Aguirre, for their continuous support, guidance, and feedback throughout my thesis. I worked on my thesis at IMEC, Energyville, and had the golden opportunity to get hands-on experience with state-of-the-art technology. I had the opportunity to work with many knowledgeable Ph.D. graduates in the field of perovskite solar cells. and they provided me with great insights at crucial junctures.

Most importantly, I would like to thank my beloved mother, father, and brother for their continuous love and support. They have been a big part of my life, and thanks to them for providing this golden opportunity to study in this great institution in the Netherlands. Further, I thank my friends who stood by me thick and thin on this journey.

Pavithran Kuppuswamy Saravanan  
Delft, August 2022

# Abstract

In 2022, the Power conversion efficiency of perovskite solar cells has achieved an efficiency of  $>25\%$ . The cost-effective and flexible perovskite-based photovoltaic has been identified as an ideal solution to increase the integration of photovoltaics in buildings. However, for a large scale implementation, the perovskite photovoltaic must perform at its best and be highly stable. The upscaling of perovskite-based solar cells to the module must be done at minimal losses.

The following research is performed on an opaque double cation p-i-n perovskite module of aperture area  $4\text{ cm}^2$ . The focus is on the laser scribing patterning technique to develop a quality interconnection in a module. The various laser parameters to be optimized and the approach to achieve a quality P1-P2-P3 scribe for the module are reported. With an ultrashort pulsed laser, the ablation of photoactive perovskite material varies remarkably. There are many possible scenarios regarding the level of ablation of  $NiO_x$  and ITO using a picosecond pulsed laser with a wavelength of  $355\text{nm}$ . In this study, the characterization concerning the emergence of contact resistance at ohmic contact is essential to identify the optimal ablation for interconnection in the module. The optimization is performed using a Scanning electron microscope in EDS mode, optical microscope, and Transmission line measurement. It helps to study the impact of different parameters on interconnection in a device.

This research shows that it is optimal to ablate beyond the HTL to completely remove the  $NiO_x$  and minimize the contact resistance. The optimized laser parameters for each scribe helped achieve an optical gain, by reducing the dead area in a module. It helped in improving the geometrical fill factor by  $3\%$ . Furthermore, the set of laser parameters also helped improve the electrical performance of a module by minimizing the drop in FF% when up-scaled from cell to module. The obtained results show an encouraging outlook for further optimization of the module by studying other laser parameters and could fast-track the up-scaling of the perovskite module with negligible interconnection and inactive area losses.

# Contents

Acknowledgements	i
Abstract	ii
Nomenclature	v
List of Figures	vii
List of Tables	ix
1 Introduction	1
1.1 Background Information . . . . .	1
1.2 Motivation and Objective . . . . .	4
1.3 Approach . . . . .	5
1.4 Structure . . . . .	5
2 Perovskite Based TFPV	6
2.1 Structural Composition and Characteristics of Perovskite Solar Cell . . . . .	6
2.1.1 Double Cation Mixed Halide Perovskite . . . . .	7
2.1.2 Inverted Perovskite Modules. . . . .	8
2.2 Cell Architecture . . . . .	9
2.2.1 Front Contact . . . . .	10
2.2.2 Hole Transport Layer . . . . .	10
2.2.3 Electron Transport Layer . . . . .	10
2.2.4 Back Contact . . . . .	11
2.3 Deposition Techniques . . . . .	11
2.3.1 DC Sputtering . . . . .	12
2.3.2 Blade Coating. . . . .	13
2.3.3 Thermal Evaporation . . . . .	14
3 Laser Processing Method	15
3.1 Laser Scribing . . . . .	15
3.1.1 Working Principle of Laser Scribing . . . . .	15
3.2 Laser system setup . . . . .	17
3.2.1 Laser Parameters. . . . .	18
4 Methodology	20
4.1 Deposition Method . . . . .	20
4.1.1 Hole Transport Layer Deposition. . . . .	20
4.1.2 Perovskite Layer Deposition . . . . .	21
4.1.3 Electron Transport Layer Deposition . . . . .	21

---

4.1.4	Metal Back Contact Deposition . . . . .	21
4.2	Processing and characterization of module . . . . .	21
4.3	Laser Scribing . . . . .	23
4.3.1	P1 Scribe. . . . .	23
4.3.2	D squared method . . . . .	24
4.3.3	P2 Scribe. . . . .	25
4.3.4	TLM measurements . . . . .	26
4.3.5	P3 scribe . . . . .	29
5	Results and Discussions . . . . .	30
5.1	P1 scribe. . . . .	30
5.2	P2 scribe. . . . .	33
5.3	P3 scribe. . . . .	42
5.4	Overview of laser parameters . . . . .	45
6	Conclusion and Outlook . . . . .	48
6.1	Conclusion . . . . .	48
6.2	Outlook . . . . .	49
	References . . . . .	53
A	Appendix 1 . . . . .	54

# Nomenclature

## Abbreviations

Abbreviation	Definition
PCE	Power Conversion Efficiency
DC	Direct Current
EDS	Energy Dispersive Spectroscopy
FF	Fill Factor
GFF	Geometrical Fill Factor
HTL	Hole Transport Layer
ETL	Electron Transport Layer
RF	Radio Frequency
PVD	Physical Vapor Deposition
TLM	Transmission Line Method
SEM	Scanning Electron Microscope
RF	Radio Frequency
UV	Ultra Violet
IR	Infra-Red
NREL	Nation Renewable Energy Laboratory
PSC	Perovskite Solar Cell
ITO	Indium Tin Oxide
TCO	Transparent Conductive Oxide
TFPV	Thin Film Photovoltaics
PV	Photovoltaics
CIGS	Copper Indium Gallium Selenide
PVD	Physical Vapor Deposition

## Symbols

---

Symbol	Definition	Unit
W	Watt	
V	Volts	
In	Indium	
Sn	Tin	
ps	picosecond	
MA	Methylammonium	
FA	Formamidinium	
Cs	Cesium	
Cu	Copper	
Br	Bromine	
I	Iodine	
L	Contact Length	$\mu m$
$L_T$	Transfer Length	$\mu m$
$R_C$	Contact Resistance	$\Omega$
$R_T$	Total Resistance	$\Omega$
$R_S$	Series Resistance	$\Omega$
$R_{Sh}$	Sheet Resistance	$\Omega$
$V_{oc}$	Open circuit Voltage	v
$W_a$	Active Area Width	$\mu m$
$W_d$	Dead Area Width	$\mu m$
kHz	Kilo Hertz	



# List of Figures

1.1	World oil consumption in every sector, 2020 [3]	2
1.2	Increase in Renewable electricity generation across technology, country and region [3]	2
1.3	Record Power conversion efficiency chart of existing PV technology developed in Lab scale,published by National Renewable Energy Lab [7]	3
2.1	Cubic Metal halide perovskite lattice structure, where A and B are cations and X is an anion [12]	7
2.2	Architecture of an planar p-i-n perovskite solar cell used in the thesis	9
2.3	Working principle of DC sputtering technology [37]	12
2.4	Working principle of Blade coating deposition technique [39]	13
2.5	Working principle of Thermal Evaporation PVD technique [41]	14
3.1	Overview of Laser scribing of a Module	16
3.2	Design of a Perovskite mini-module	16
3.3	Side view of the Laser Setup near the Chuck Area [43]	17
3.4	Schematic representation of laser surface employing a line scribe strategy to demonstrate a parameter laser pulse overlap (PO)[45]	19
4.1	Overview of inverted opaque perovskite module fabrication	22
4.2	Gaussian beam profile at laser and material interaction spot [49]	24
4.3	Ablation threshold fluence determination according to $D^2$ method [50]	25
4.4	TLM Schematics used for determining P2 contact resistance and sheet resistance of ITO [52]	27
4.5	Arrangement of TLM test pattern, where blue and grey areas are film and contact respectively [53]	27
4.6	Least resistive Current transfer path between metal back contact and semiconductor [54]	28
4.7	Fit plot to derive Transfer length and sheet resistance from TLM method [54]	28
4.8	Overview of sample preparation for TLM measurements	28
5.1	Absorptance spectrum of the commercial ITO	30
5.2	A series of parallel P1 scribes at power 260 MCS and at scribe speeds from 100 mm/s at bottom to 500 mm/s at top	32
5.3	Microscopic image of ablation depth when scribed at 260 MCS and 300 mm/s for P1 scribe	32

5.4	Elemental composition of the P1 scribe at power 260 MCS and scribe speed 300 mm/s using EDS scan . . . . .	32
5.5	SEM image at 3600x magnification for P1 scribe at power 260 MCS and scribe speed 300 mm/s . . . . .	33
5.6	Elemental composition of the P1 scribe at power 260 MCS and scribe speed speed 300 mm/s using EDS scan . . . . .	33
5.7	Absorbance spectrum of the perovskite cell architecture . . . . .	33
5.8	$D^2$ of ablated spot in $\mu m^2$ vs pulse energy (J) for determination of $NiO_x$ ablation threshold fluence . . . . .	34
5.9	$D^2$ of ablated spot in $\mu m^2$ vs pulse energy (J) for determination of ITO ablation threshold fluence . . . . .	34
5.10	Parallel scribes for power scan experiment with increasing fluence from left to right . . . . .	35
5.11	Elemental composition at each scribe under SEM in EDS mode . . . . .	36
5.12	Elemental composition at each scribe under mapping mode . . . . .	36
5.13	Electrical performance of modules with P2 scribes at different fluences . . . . .	37
5.14	Design of TLM devices used for line contact P2 interconnection [52] . . . . .	38
5.15	Transmission line measurement at lower fluence $110mJ/cm^2$ . . . . .	38
5.16	Transmission line measurement at higher fluence $440mJ/cm^2$ . . . . .	38
5.17	Plot of Contact Resistance against contact length at different fluences . . . . .	39
5.18	Plot of Contact resistivity against contact length at different fluences . . . . .	39
5.19	Plot of transfer length against contact length at different fluences . . . . .	40
5.20	Plot of transfer length against contact length at fluences $110mJ/cm^2$ and $440mJ/cm^2$ . . . . .	40
5.21	Module performance at different P2 width for fluence $110 mJ/cm^2$ and $440 mJ/cm^2$ . . . . .	41
5.22	Depth profiling of P2 scribe spot and scribe line under optical microscope . . . . .	42
5.23	P3 scribe before optimization under SEM . . . . .	42
5.24	P3 scribe after optimization under SEM . . . . .	42
5.25	Parallel scribes at power from 210 MCS to 320 MCS under SEM . . . . .	43
5.26	P3 scribes at different power from 250 MCS at top to 280 MCS at bottom under optical microscope . . . . .	43
5.27	Elemental composition of P3 scribe under SEM in EDS mode . . . . .	44
5.28	Elemental composition of P3 scribe under SEM in EDS mode . . . . .	44
5.29	The scribe design before laser parameter optimization . . . . .	45
5.30	The scribe design after laser parameter optimization . . . . .	45
5.31	Performance data of cell (left) and module (right) before laser parameter optimization . . . . .	46
5.32	Performance data of cell (left) and module (right) after laser parameter optimization . . . . .	46
A.1	Design of single cell and mini-module used in the thesis [52] . . . . .	54
A.2	JV plot of modules in figure 5.13 . . . . .	55
A.3	JV plot of modules with P2 scribe fluence $110mJ/cm^2$ and at different contact length . . . . .	56
A.4	JV plot of modules with P2 scribe fluence $440mJ/cm^2$ and at different contact length . . . . .	57

# List of Tables

5.1	Insulation test for scribes of power scan experiment . . . . .	31
5.2	Ablation Threshold fluence parameters for $NiO_x$ and ITO layers ablated with UV laser . . . . .	35
5.3	Laser parameters of each scribe line . . . . .	45
5.4	Optimized parameters of P2 scribe . . . . .	45
5.5	Relative drop in performance after upscaling . . . . .	47
A.1	TLM measurements at different fluence and Contact length . . . . .	58

# Chapter 1

## Introduction

This chapter aims to provide an introduction to this thesis and the main objective and motivation for pursuing this thesis project. In Section 1.1, the necessity for increasing solar energy is discussed. Moreover, this chapter also highlights why perovskite-based solar cells are the future. The motivation for working on this project is in Section 1.2. In Section 1.3, the focus is on the project's main goals and the approach to achieving this objective. Finally, in Section 1.4, the format of the report is elucidated.

### 1.1 Background Information

As per current records, the human population has increased to around 7.9 billion. The main reason for this increase in population is the progression in energy, science, and technology. The broader picture shows that population increase goes hand in hand with energy usage globally. At the same time, this sudden demand for energy has led to the over-consumption of fossil fuels. In the past decades, the increase in primary energy usage has been higher than the total final energy consumption [1]. It proves that energy consumption worldwide has been increasing without any noteworthy developments in energy conversion. Overall, it has had adverse effects on climate change across the globe.

In recent years, climate change has been severe due to the burning of fossil fuels, leading to an increase in the concentration of greenhouse gases and in global atmospheric temperature [2]. Among the natural resources, oil is a majorly consumed natural resource. As per figure 1.1, oil has been mainly consumed in the transport sector, followed by industry and other sectors worldwide. However, the increase in fossil fuel consumption has reached a saturation point in the energy industry. Civilizational developments are needed in every sector to minimize atmospheric issues, and it is of utmost importance to create a sustainable environment in the future.

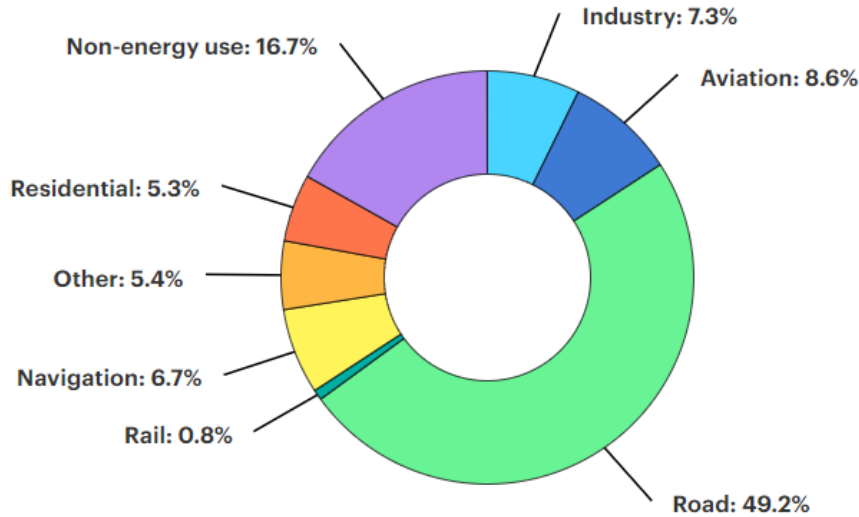


Figure 1.1: World oil consumption in every sector, 2020 [3]

The increase in demand for sustainable energy has stipulated the need for more renewable energy-based technologies on a larger scale. In recent years, various efficient renewable energy technologies have been developed to cover the energy demand of the entire globe more productively. This recent increase in renewable electricity generation across technology and country is shown in figure 1.2. However, according to recent research, 29% of world electricity will be generated from renewable energy sources like solar and wind at the end of 2020 [4].

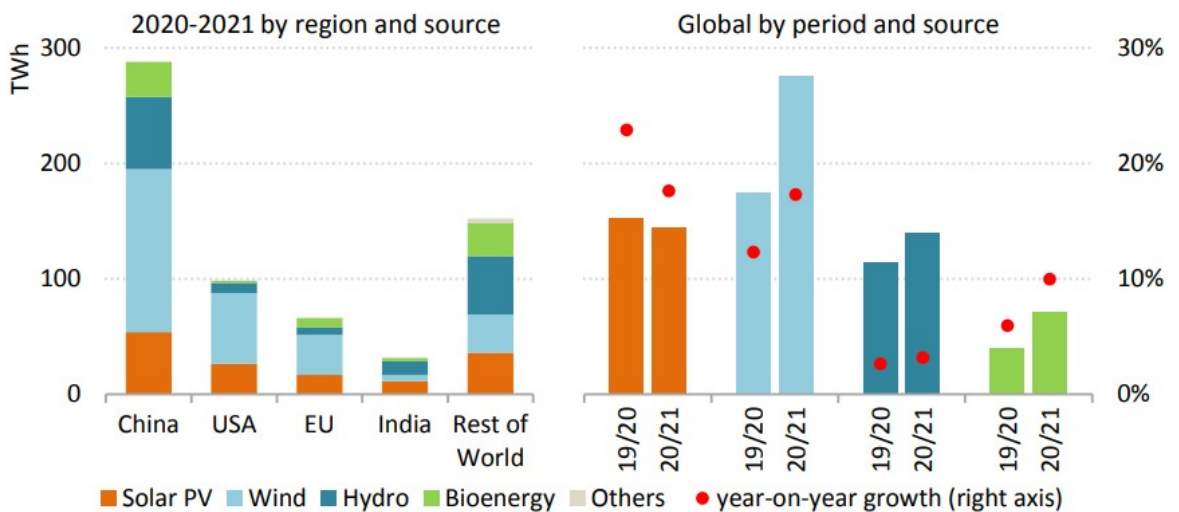


Figure 1.2: Increase in Renewable electricity generation across technology, country and region [3]

One such prominently available source of renewable energy is solar energy, which can easily cover the global energy demand. In addition, to utilize solar energy with minimal loss and constraint, PV technology has been used. The mainstream PV technology uses crystalline silicon wafers as the absorber material. In the past decade, \$1.3 trillion has been invested in PV technology to escalate the installed capacity of PV technology all across the globe [5]. With the increase in capacity, there has been a drastic drop in the price of PV technology. It has made the PV system more feasible and could easily be implemented in many small-scale devices to large-scale utilities without many constraints. With all these advantages in place, there has always been a motive of fully utilizing the solar energy delivered to the earth’s surface as it can cover the global annual energy demand. More research is done to improve the power conversion efficiency of different PV technologies existing in the market to utilize its vast potential.

There are numerous types of PV technology currently available in the market. However, among the different types of PV technology, the current market is dominated by silicon-based PV technology at 95%, followed by CI(G)S and CDT, which together account for the remaining 5% and are so-called thin film PV(TFPV) technologies [6]. The industry’s current dominance and reliance on silicon-based solar cells are due to their established processing technique and abundance of pure silicon and bandgap. However, the presence of an indirect bandgap causes the loss of cells. It has stalled the improvement of the efficiency of silicon-based solar cells. Moreover, as per current records, the power conversion efficiency of a single crystalline, multi crystalline silicon, and multi-junction solar cell stand at 27.6%, 23.3%, and 47.6%, respectively. In the below figure 1.3, the record power conversion efficiency of currently available PV technology are shown.

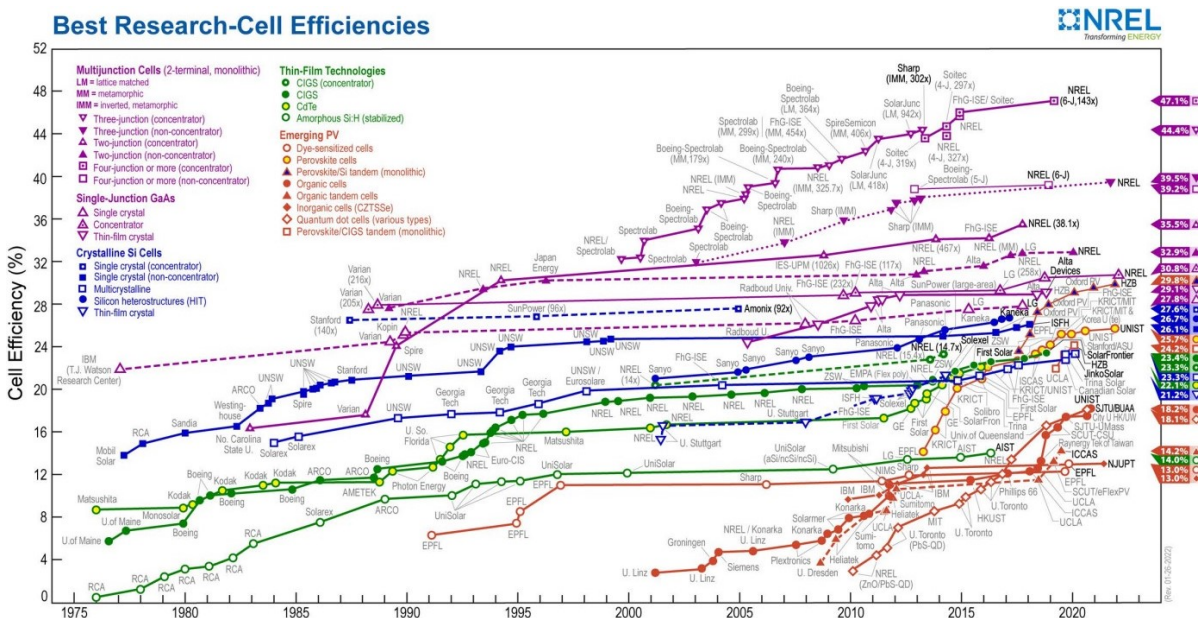


Figure 1.3: Record Power conversion efficiency chart of existing PV technology developed in Lab scale, published by National Renewable Energy Lab [7]

With silicon-based PV technology steadily approaching its theoretical PCE limit, it has created a need to develop new thin-film PV technologies suitable for multiple applications and with higher PCE. The new thin-film technology to be developed must be upgraded to overcome all these challenges of existing PV technology. Moreover, some already existing thin-film silicon technologies are highly flexible, transparent, lightweight, and offer a solution for building integrated photovoltaic because of their uniform appearance [8]. However, they also fail to achieve high power conversion efficiency [8]. So to uphold all these characteristics and overcome some challenges, a technology named Perovskite-based TFPV has been developed that achieves high efficiency in addition to the advantages of other thin-film technologies. It is fast approaching to be one of the most prominent and developing PV technology that can be flexible and efficient enough for multiple applications. Further, the PSCs are used in tandem cells with existing technologies to generate higher power conversion efficiency of around 31.25%.

According to the National Renewable Energy Laboratory (NREL) 2022, the highest achieved PCE at lab scale is about 25.7% for perovskite based solar cells [7]. Recently, tandem cells with perovskite and silicon has achieved an efficiency of 31.25% [9]. However, the main challenge of up-scaling these perovskite-based solar cells to commercialization persists. To upscale this TFPV, a scribing technique is used to develop interconnection between cells in a module. The scribe pattern can be performed either mechanically or by using laser system. This project uses the laser scribing technique to upscale the opaque inverted perovskite cells into modules by optimizing the laser parameters and technique for processing these scribes.

## 1.2 Motivation and Objective

The research goals were defined after the literature study. The primary motivation of this thesis is to upscale opaque p-i-n perovskite solar cells by studying the patterning technique that helps perform this upscaling operation. The initial study involved understanding the P1-P2-P3 scribes, their functionality, and the methods to fully optimize the scribe. Most of the earlier research was on silicon cells, n-i-p perovskite solar cells, and semitransparent cells.

Furthermore, the upscaling of p-i-n perovskite solar cells is a new challenge, and it can be done by two patterning techniques: mechanical scribing and laser scribing. The laser scribing technique helps develop a quality interconnection necessary to achieve a highly efficient mini-module. Hence, the laser scribing technique and parameters are studied and optimized using different techniques. Also, it provides a detailed understanding of the interconnection of modules. The study on this technique helps understand the interconnection method's effect on these modules' electrical performances and the losses involved while upscaling a cell.

Certain research questions are mapped out to achieve the final objective of the thesis:

- How to retain the electrical performance of inverted perovskite-based solar cells when upscaled with minimal losses
  - What are the different techniques for optimizing the scribe pattern?
  - What are the important laser parameters to be optimized?
  - How does the quality of the scribe impact the electrical performance?

The project's main objective is to study the effect of the laser scribing technique on perovskite mini-module performance. The laser parameters associated with the tool used to perform the scribe operation are optimized to perform a quality P1-P2-P3 scribe operation. The optimized P2 scribe pattern helps study the effect of total module resistance at the ohmic contact. The thesis aims to evaluate the impact of developed interconnection on the electrical performance of these modules. Moreover, the aim is also to minimize the inactive area and interconnection losses.

## 1.3 Approach

Approaches to achieve the final objective:

- Devising a course of action to optimize the P1-P2-P3 scribe
- Evaluating the impact of developed interconnection on the electrical performance of these modules
- Minimization of the inactive area and interconnection losses

The approach taken to achieve these goals is by individually optimizing the laser parameters for each P1-P2-P3 scribe. The optimized parameters help to have a quality interconnection between the modules' cells and fulfill their objective. The quality of the scribe is further analyzed using qualitative and quantitative measurement techniques, namely SEM in EDS mode, optical microscope, and Transmission line measurement. The quantitative analysis helps understand the impact of module resistance on interconnection and assists in understanding other parameters, which aids in optimizing the scribe pattern and width. This way, it helps analyze certain losses, namely the inactive area losses and interconnection losses in modules. To conclude, the drop in performance from a cell to a module for different laser scribe parameters is analyzed by comparing the electrical performance between a module and a cell for the same cell architecture.

## 1.4 Structure

The report's structure follows a detailed introduction to perovskite material, its cell architecture, and the working principle in chapter 2. Followed by this, a detailed overview of the laser processing method, the tool setup, and its parameters are described in Chapter 3. Chapter 4 gives an in-depth explanation of the processing methodology. Chapter 5 will enlist results of the experiments. The overall conclusions and recommendations for further research are given in Chapter 6. Chapter 7 contains the summary of the thesis.



# Chapter 2

## Perovskite Based TFPV

This chapter describes the hybrid metal halide perovskite and its structural composition in section 2.1. Additionally, the architecture of an opaque perovskite solar cell is explained. Finally, the material employed for each layer and its functional purpose is elucidated in section 2.2.

### 2.1 Structural Composition and Characteristics of Perovskite Solar Cell

The hybrid metal halide perovskites are pivotal in delivering the next generation of affordable, flexible, and high efficient PV technology. This semiconductor is used as photoactive material in perovskite-based TFPV technology. Extensive research has been performed to fully utilize the potential of organic-inorganic metal halide perovskite. It has been used as a light absorber in solid-state thin film perovskites [10]. The perovskite-based solar cell comprises of an organic-inorganic lead or tin halide substance. As mentioned above, it acts as an absorber and a charge carrier conductor.

The modern perovskite material consists of a chemical structure with the  $AMX_3$  formula (commonly known as  $ABX_3$ ). The organic or inorganic monocation (typically methylammonium [MA], formamidinium [FA], and cesium [Cs]) occupies site A. Whereas a dication occupies the M site (typically lead or tin) and the X site is occupied by a halide (iodide, bromide, or chloride). The different cations and anions in the lattice are of various dimensions. However, because of their excellent interactions with each other, it is being made possible to form a stable 3D perovskite structure [11]. The overall crystal structure of methylammonium lead halide perovskite  $CH_3NH_3PbX_3$  (X=I, Br or Cl) is depicted in the figure 2.1.

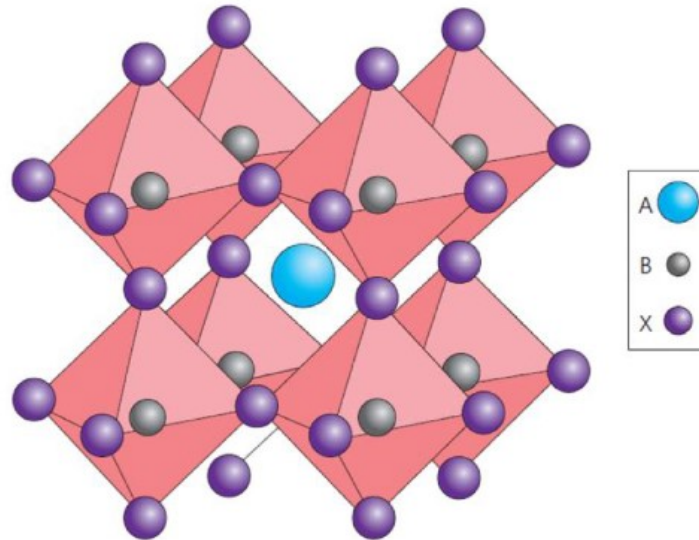


Figure 2.1: Cubic Metal halide perovskite lattice structure, where A and B are cations and X is an anion [12]

The perovskite-based material has a tunable bandgap range from 1.6 to 2.3 eV. It can be modified by varying the chemical composition of perovskite. It is done by switching cations on the MA site and anions on the halide site to their desired value for multijunction [13]. Along with tunable bandgaps, perovskite solar cells have witnessed tremendous improvements in PCE since 2009, mainly due to the superior photophysical properties that govern their functionality, namely, low binding energy, long carrier diffusion length, and photo-generated charge separation [14]. The PSC plays a major role in optoelectronic applications. It has a unique lattice nature, and optoelectronic characteristics [15]. It varies based on the chosen material. Moreover, they are majorly used in PV applications because they exhibit high optical absorptivity, have outstanding structural defect tolerance, lower surface recombination, and favorable grain boundary effects [14][15][16]. These characteristics are the reason behind the ever-improving efficiency of these hybrid metal halide perovskite [17][18].

### 2.1.1 Double Cation Mixed Halide Perovskite

The photoactive perovskite layer can act either as a sensitizer or transport layer [19]. This layer is deposited over the hole transporting layer. The cations and anions used in photoactive layers impact the overall performance of the modules. Despite their current high PCE, these perovskite-based solar cells suffered from photo-and/or moisture instability, hindering their development [20]. It was mainly due to the weak interaction between different sized organic cation at A site and anion at X site and also due to the chemical non-inertness of organic cation [20]. In recent years, the organic and inorganic perovskite has reached a PCE of 25.7% [21]. However, over the years, the composition of perovskite has varied drastically to procure a cell with better performance and stability. The most commonly used perovskite was  $MAPbI_3$ . However, a shift happened towards  $FAPbI_3$  as it was found to be that a reversible phase transition occurred at room temperature when  $MAPbI_3$  was employed [20]. It directly affected the photo and

thermal stability of perovskite-based solar cells. However, there was an issue with the presence of humidity [20]. Later, approaches were taken to instill methyl-ammonium with Formamidinium to combat the humidity issue. But this resulted in low thermal stability, and the perovskite film also had stability issues in the long term [21].

There have been numerous research on double cation perovskite involving Formamidinium (FA) and cesium (Cs) for the improved understanding of humidity and long-term stability issues. The infusion of non-organic Cs in the perovskite composition with organic Fa has improved the photo-and/or moisture stability [20]. This is due to the contraction of structure volume, which facilitated enhanced interaction between cation and anion [20]. In addition, the incorporation of  $Cs_+$  inorganic cation has drastically reduced the trap density, directly impacting the electrical performance of the cells [20]. This thesis uses a double cation recipe as a perovskite layer involving FA, Cs, and Pb for respective A and B cation sites.

At the same time, the X site is occupied by halide ions, namely Iodine and Bromine. The research behind the halide composition considers many parameters as it needs to meet the demand for both single junction and tandem solar cells. The implementation of mixed halide is mainly down to the ability to tune the optical band gap of materials by varying the elemental composition ratio of Bromine and Iodine [22]. This in turn helps in achieving higher PCE for perovskite-based solar cells and tandem devices. Moreover, by altering the Br-I ratio, the bandgap of respective perovskite can be fine-tuned from about 1.6eV to 2.3eV [22]. The perks of having a mixed halide perovskite are that it makes the device strongly stable against humidity and thermally stable, and it also helps in improving the electrical performance of the device by increasing the  $V_{oc}$  and FF for a Br ratio ( $x < 0.2$ ) [22]. On the downside, if the Br ratio exceeds ( $x > 0.2$ ), it decreases the  $V_{oc}$ ; this is ideally due to the light-induced phase segregation as both the anions under light excitation begin to segregate [22][23]. The halide ratio used in this research is 0.947 for Iodine and 0.053 for Br. However, the overall perovskite composition is  $Cs_{0.2}FA_{0.8}Pb(I_{0.947}Br_{0.053})_3$  and the bandgap of the respective recipe is 1.60 eV. Further, the below section discusses the device architecture in which the double cation mixed halide perovskite is used.

### 2.1.2 Inverted Perovskite Modules

The Perovskite-based solar cells can be classified based on the structure of the layers, either planar or mesoporous [24]. The planar structure can be further divided into two types based on the arrangement of layers in the stack, namely, regular n-i-p and inverted p-i-n structure [24]. These configurations are named based on which transport material layer gets first in contact with incident light. In this structure, p represents a hole transport layer, i represents the intrinsic perovskite layer, and n represents the electron transport layer. In recent years after several developments, the regular n-i-p structure has achieved a power conversion efficiency of over 25.7% [25]. Simultaneously there have been various kinds of research done with the inverted structure, and they have shown staggering results in terms of stability, device performance, ease in fabrication, and its ability to suppress the hysteresis effect [26]. Also, these devices are cost-effective to

develop. Recently an efficiency of around 23.72% has already been achieved for the respective solar cell structure [25]. These PSCs have the potential to achieve higher efficiency. The primary purpose of utilizing the p-i-n structure in this research is its feasibility to upscale.

## 2.2 Cell Architecture

The perovskite-based solar cell has layers stacked on top of each other, namely transparent conducting oxide, hole transport layer, the absorber layer, electron transport layer, and back contact. The PSC stack is shown below in figure 2.2. These layers are pivotal for obtaining good electrical performance where the ETL acts as a hole blocking layer and HTL acts as an electron blocking layer to segregate the hole and electron generated in the photo-active layer. Further in this thesis, the focus is mainly on planar p-i-n perovskite structure. In the planar perovskite solar cell, the mesoporous scaffold layer between HTL and ETL is eliminated and only the perovskite layer is present [27]. All research and analysis in this thesis are done on this configuration where the incident light first passes through the hole transport layer. Further, the different layers of the perovskite module and its functionality are discussed below.

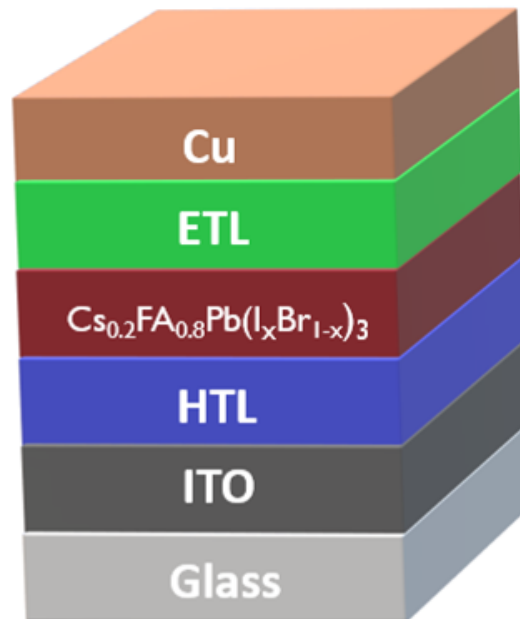


Figure 2.2: Architecture of an planar p-i-n perovskite solar cell used in the thesis

### 2.2.1 Front Contact

The transparent conductive oxide (TCO) is used as a front electrode in the stack. It behaves as a transparent electrode that receives photons into the perovskite-based solar cell. Indium tin oxide (ITO) is used as TCO in perovskite-based solar cells. This decision is made based on its property of low resistivity, and high transparency [28]. Further, the ITO with a bandgap of 3.5-4.5 eV is sputtered on the glass substrate with a thickness of 150nm. This helps to reduce the parasitic absorption [29]. Moreover, it also helps absorb light in the visible and infrared spectrum when it is oxidized. These particular properties were the reasons behind implementing commercial ITO as front contact.

### 2.2.2 Hole Transport Layer

The hole transport layer, which acts as a P-type semiconductor, performs the role of hole collector and blocks electrons. In recent years, there has been a trend with Spiro-OMeTad being replaced by  $NiO_x$  as the hole transport layer in the hybrid metal halide inverted perovskite solar cells [30]. This change has occurred due to the superior long-term stability of inorganic materials and ideal band alignment with perovskite structures [30]. The shift occurred based on results that proved the instability of Spiro-OMeTad and due to the development of voids [31]. As a result  $NiO_x$  has become a viable alternative by overcoming all the drawbacks of organic HTL. The intrinsic Ni vacancies assist with the conductivity of holes in  $NiO_x$  semiconductor [32]. Also, the  $NiO_x$  has a superior hole extracting capability from perovskite. This property helps restrict the recombination of photogenerated electrons and holes in perovskite [32]. Furthermore, the  $NiO_x$  is deposited as the hole transport layer by DC sputtering in this thesis .

### 2.2.3 Electron Transport Layer

On top of the photoactive layer, an electron transport layer is directly deposited to block holes and transport electrons. As it is critical, several criterias must be contemplated for the choice of ETL for inverted perovskite solar cells. The main considerations are the impact of ETL on the perovskite layer, the level of electron mobility, hole blocking capacity, and the complete layer coverage [24]. In the ETL stack, the most important component is the fullerene-based material  $C_{60}$ . The respective component secures the charge separation, higher mobility, and conductivity and ensures the device performs at its fullest capacity [24]. For the ETL to perform its function efficiently, the fullerene material faces a challenge between film coverage and electron transport. The developed  $C_{60}$  needs to be thin enough to establish sufficient electron transporting capacity with minimal resistance, but this also creates a situation where it does not cover the entire perovskite film [33]. It leads to contact between perovskite and back contact, possibly leading to current leakage.

Moreover, additional functional layers are deposited with the fullerene-based materials to form an ETL stack. A thin layer of LiF is deposited. The generated layer reduces the energy barrier height by creating a dipole moment at the interface of the electron transport layer, and the back contact [33]. The thickness of the LiF layer ranges from 0.8 to 1 nm. This reduces the contact resistance between back contact and the  $C_{60}$  layer,

and it provides better electron transport that helps in improving device performance [33].

In addition, the ETL employed for the inverted perovskite solar module has a hole blocking layer. It minimizes nonradiative recombination at the ETL-Cu interface [33]. Bathocuproine (BCP) is a buffer layer between C60 and back contact. The thin layer creates an ohmic contact between C60 and the Cu back electrode in the perovskite solar module stack [33]. Including a buffer layer improves PSCs' performance by providing long-term stability [34]. All the above mentioned ETL layers are deposited by thermal evaporation and it finalizes the ETL stack of the perovskite solar cell to be used in this thesis.

#### 2.2.4 Back Contact

The fabrication of the module is completed by developing a back electrode on top of the ETL. As discussed in an earlier section 2.1.2, to develop an opaque perovskite module, a metal back contact is to be utilized as the back electrode. Cu is chosen over other metals like Au, Ag, Al and Ca as the back electrode, because of its slow degradation when illuminated continuously for a longer duration [35]. The Cu metal is highly stable for a long time in both scenarios of being in direct contact with perovskite and having an ETL deposited between the photo-active layer and back electrode.

Also, The Cu metal has proven to be a stable electrode for flexible high efficient perovskite modules as it defers to affect the electrical performance of the module, unlike other metals [35]. Another essential criteria behind utilizing a Cu metal as the back electrode is its low diffusion into perovskite as maintaining the stability of perovskite has been the main challenge [35]. This prove that these cost-effective Cu back electrode promises to be a long-term solution for perovskite solar modules. In this research, the Cu metal is deposited by the thermal evaporation technique to develop a uniform layer of thickness around 100nm. The deposition of the back electrode completes the cell stack. In the below chapter 3, the laser technology implemented for making the scribe pattern is discussed in detail.

## 2.3 Deposition Techniques

The most commonly used fabrication strategies are vapor-assisted processing and wet chemistry processing. The wet chemistry processing is divided into one-step and two-step sequence deposition techniques and is primarily used in lab scale experiments [36]. Whereas vapor-assisted processing techniques are used for processing large area perovskite. Moreover, there are different processing strategies: thermal vapor deposition, roll-to-roll fabrication technique, inkjet printing, slot-die coating, spray-coating, spin coating, and blade coating [36]. The different techniques have different effects on the film morphology of the perovskite.

Moreover, different fabrication techniques are studied to understand the perovskite crystallization process [36]. It helps to decide on the most optimal fabrication technique for processing large area perovskite. The final performance is entirely dependent on

the quality of the film. On top of this, further study is necessary to fathom the commercialization of perovskite devices. In the below section, the working principle of the deposition technique to be used in this thesis is discussed.

### 2.3.1 DC Sputtering

In a perovskite-based module, a thin film is deposited by the magnetron sputtering technique. It is a thin-film vapor deposition technique widely used to deposit TCO (ITO). The working principle of the magnetron sputtering technology is to enhance the electron motion of the target under a magnetic field [37]. In the tool setup, the direct current powers the target material as the used target is conductive. It can also be powered with radio frequency (RF) when using a non-conductive target [37]. However, the former is preferred due to its economic feasibility and operability [37]. The DC sputtering technique generally uses a source material called the target material, placed in a vacuum chamber parallel to the substrate. The respective chamber is vented to remove the H<sub>2</sub>O and H<sub>2</sub> and later pumped down with inert gas argon.

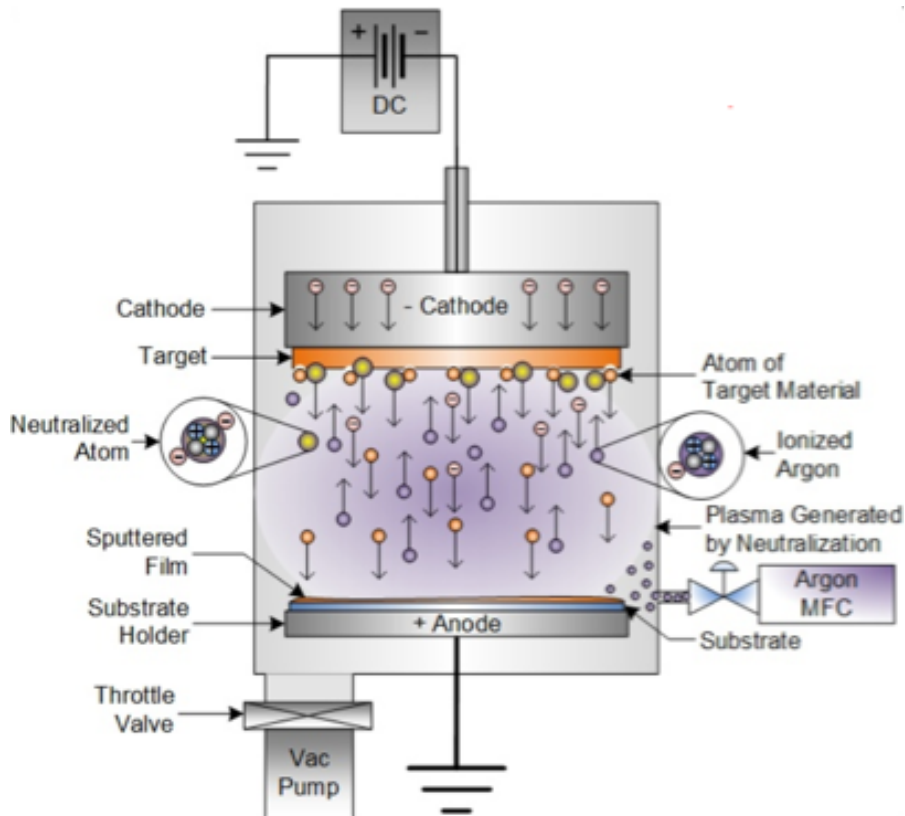


Figure 2.3: Working principle of DC sputtering technology [37]

The sputtering method begins with a collision of an argon atom with an existing free electron in the vacuum chamber, which revolves around the negatively charged target material under the magnetic influence [38]. The electron develops an ionized atom by ejecting an electron from the argon atom. Moreover, the electrons and positive ions generated in the plasma of magnetically enhanced glow discharge provide an impetus for deposition [38]. Further, the positive ion is pulled towards the negatively charged target with great force, and the target material's bombardment with ionized gas molecules causes vapor [38]. It mainly depends on their capability to transfer kinetic energy upon collision. This physical process performs the sputtering of the source material. The collision of an ionized atom with a target material releases an atom from the target material, which travels across the vacuum [37]. Later, when the vaporized atoms condense, they are deposited as thin films on the surface to be coated. As a result, the substrate is coated uniformly with the desired target material.

### 2.3.2 Blade Coating

The blade coating technique has been preferred for depositing the photoactive layer on top of HTL in this thesis. In a vacuum chamber, a sharp blade is placed alongside the substrate surface at a fixed distance to develop a layer with uniform thickness [39]. Then, the prepared perovskite solution is placed in the sight of the sharp blade. Further, the blade is moved across in line with the substrate surface, and the developed wet film is dried.

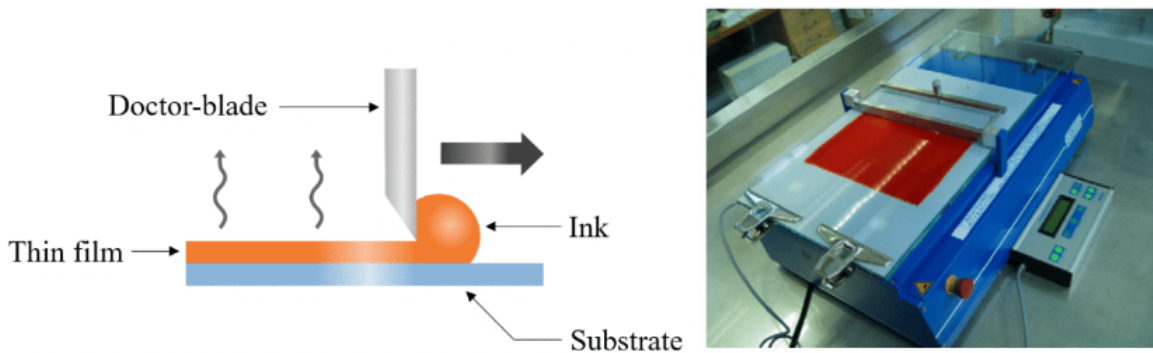


Figure 2.4: Working principle of Blade coating deposition technique [39]

The developed perovskite film thickness is equivalent to the fraction of the gap between the substrate and the blade. In this process, the coating speed and viscous properties of the solution also influence the final thickness of the deposited film [40]. Moreover, in comparison with spin coating, the blade coating technique saves material and is suitable for the large-scale coating that allows upscaling perovskite-based solar cells [40]. This is the reason behind using blade coating technique for depositing the photoactive layer in this thesis.



### 2.3.3 Thermal Evaporation

Thermal evaporation is another physical vapour deposition technique that develops films on substrate at a thickness range from angstroms to microns. The developed thin film can be either be a metal or a non metal, oxides and can even be a single or multiple material in a layered structure. The flexible deposition technique performed in a closed vacuum chamber involves heating a solid material that is located at the bottom of the chamber, to a temperature that is around the melting point of the material [41]. This develops some vapour pressure. The developed vapour cloud rises inside the closed vacuum chamber even at a low vapor pressure. The evaporated material travels across the chamber in the form of vapor steam with some thermal energy and coats the substrate that is held on top side facing downwards. This system offers high deposition rate and manages the thickness of coating adequately [41]. The metal back contact deposition for PSC is done using thermal evaporation in this thesis.

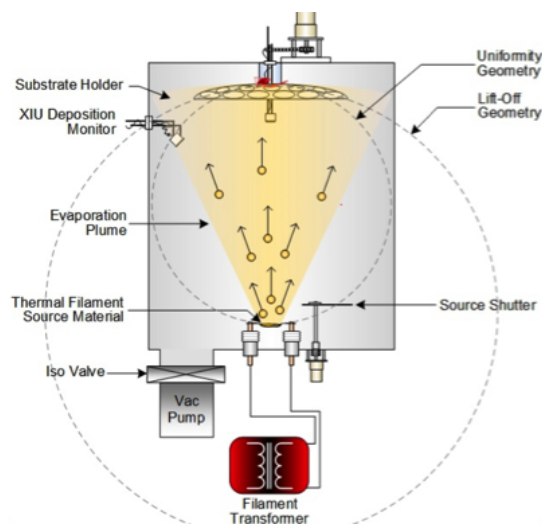


Figure 2.5: Working principle of Thermal Evaporation PVD technique [41]

# Chapter 3

## Laser Processing Method

This chapter aims to describe the laser processing method. The working principle of the laser scribing technique is discussed in section 3.1.1. In section 3.2, the laser system setup and its components are briefly discussed. Finally, the necessary laser parameters and science behind laser-material interaction are elaborated in section 3.2.1.

### 3.1 Laser Scribing

The upscaling of the cell to a module is performed with the help of different patterning techniques, namely, mechanical, laser patterning styles and-so-forth. However, the latter is preferred over the former. It is mainly due to the superior features the laser has to offer. The scribe technique assists in developing flexible, versatile, precise and repeatable modules irrespective of the substrate, deposited layers, and pattern design. The scribe operation is performed with an ns or ps pulsed layer. The above method helps to perform the P1-P2-P3 scribe that develops an interconnection between cells in a module.

#### 3.1.1 Working Principle of Laser Scribing

Initially, the P1 scribe is done on the ITO layer, which insulates the front electrodes of adjacent cells electrically [42]. Secondly, the P2 scribe is the most critical scribe pattern as it helps in creating an electrical contact between the front and back electrodes of adjacent cells in a module. The P2 scribe selectively ablates all the layers above ITO performed after deposition of HTL, perovskite layer, and ETL. Further, the developed ohmic contact helps transfer the gathered photo-generated current from one cell to another [42]. Finally, the P3 scribe is done following the deposition of back contact to isolates the different cells in a module [42]. In the below figure 3.1, both the side view and top view of the scribing performed on a module are shown, where a perovskite module has four cells interconnected in the series pattern and with a cell length of  $L$ .

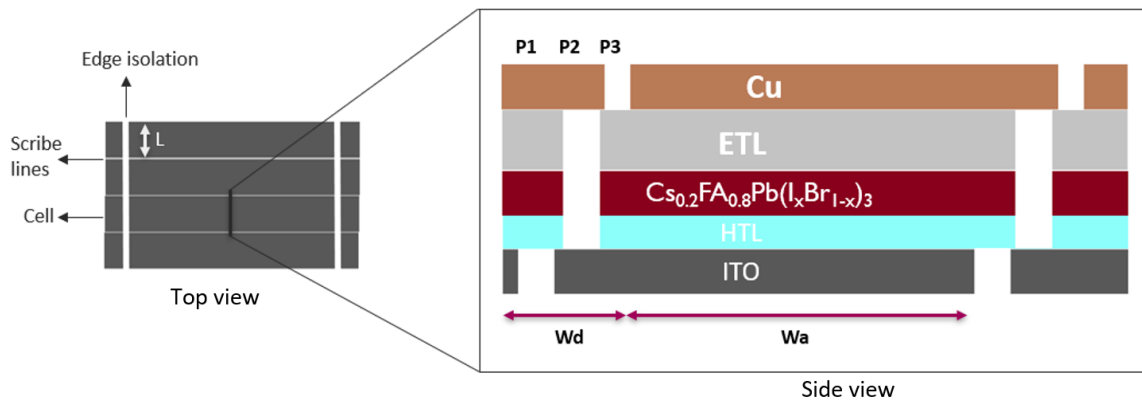


Figure 3.1: Overview of Laser scribing of a Module

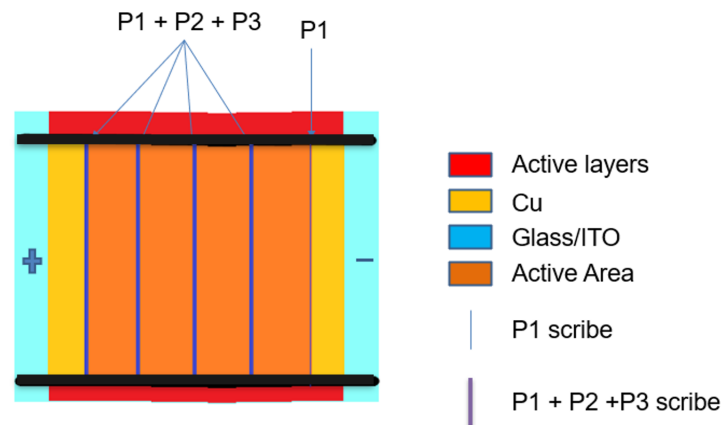


Figure 3.2: Design of a Perovskite mini-module

The interconnection technique has some losses involved with it. The developed laser patterns of the modules should be optimized to minimize these interconnection losses. The distance between the edges of P1-P3 scribe in a module are renowned as dead area (DA), which are allocated for interconnection between adjacent cells, and these regions fail to contribute to energy conversion [42]. Whereas the areas excluding the dead area are known to be the active area (AA), where the mechanism of photo generation of charges and energy conversion takes place in a module [42]. Finally, after the scribing operation, the main parameter obtained from the module cross section is the Geometrical Fill Factor (GFF). This factor is the ratio between the active area (AA) and the aperture area (AR), where the aperture area (AR) is the sum of the dead area and the active area [42]. This parameter calculates the electrical performance of a module in the active area.

## 3.2 Laser system setup

The laser tool implemented for scribing thin-film PV is M-Solv700. The tool can handle perovskite-based mini-modules of sizes up to 350 x 350 mm size. The perovskite-based mini-modules are protected from external moisture by performing the laser scribing operation in a glove box. The glove box has an attached load-lock antechamber. This chamber is maintained at  $<1$  ppm O<sub>2</sub> and H<sub>2</sub>O to avoid degradation of cells [43]. The laser tool for scribing the cells uses a ten ps-pulsed diode laser with three available wavelengths. It comprises of an Infrared (1064nm), Green (532 nm), and UV (355 nm) laser.

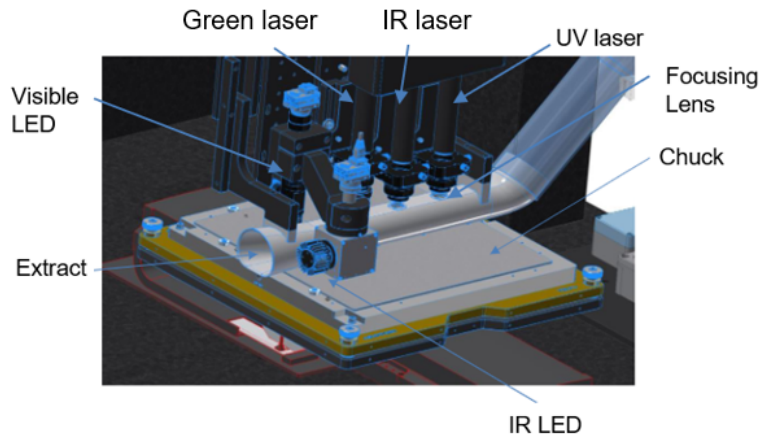


Figure 3.3: Side view of the Laser Setup near the Chuck Area [43]

The laser tool has a repetition rate of up to 2000kHz and has a maximum power output of 29W at 1064 nm wavelength [43]. These are some predefined set specifications retrieved from the laser tool manual. Further, to perform the laser scribe operation the laser beam is directed onto the workpiece, and the chuck holds the workpiece. The chuck uses a split axis gantry x-y stage with set parameters that helps in the movement of the laser scribing process. Moreover, the tool also uses a focusing lens mounted on a Z stage of the system that accompanies in focusing of the laser beam onto the workpiece [43].

The laser tool uses a convertible optic system with software that helps adjust the spot size of the laser beam and the pulse energy. Then, the laser beam is moved across the chuck using open software to process a scribe on the workpiece. Additionally, the tool has an inbuilt debris extract system to maintain a stable environmental system for perovskite modules by filtering the debris after scribing using a vacuum unit. The scribe operation is done with the help of two camera systems mounted on the z stage, namely an infrared and a visible light camera [43]. It helps with viewing the workpiece, performing scribe patterns, and aligning scribes using a monochrome camera with low magnification. The whole M-Scan system that runs with software helps with a system command issued by a Python script. The software has multiple laser parameters, which are modified according to the type of scribe needed. The different laser parameters optimized in this thesis for different scribes are discussed in the below section 3.2.1.

### 3.2.1 Laser Parameters

A quality scribe is performed with a laser tool by optimizing certain parameters. Certain parameters that need the attention are the wavelength (nm), pulse length (ps), frequency (kHz), apparent power (MCS), scribe speed (mm/s), stage height (mm), Laser pulse overlap (O), Pulse Energy (J), Fluence ( $J/cm^2$ ), ablation threshold fluence ( $J/cm^2$ ). These parameters are optimized when performing laser processing. Initially, when an incident beam of electromagnetic radiation is directed onto a sample, it excites the electron from a lower to a higher energy level. This happens due to the monochromatic laser light's high power density and directionality [44]. Following this, in a short period, the charged particles with high energy levels dissipate energy in the form of heat. It is the energy utilized to perform the action of ablation on a material [44].

$$PulseEnergy(J) = \frac{Power(W)}{Frequency(kHz)} \quad (3.1)$$

$$Fluence(J/cm^2) = \frac{PulseEnergy(J)}{AreaofSpot(cm^2)} \quad (3.2)$$

The laser tool setup uses a preset pulse length in pico-seconds, ultra-short pulses. The main advantage of these ultra-short pulses is their high quality and reproducibility. As the pulse duration or length increases, it develops a thermal effect on the material to be ablated [44]. Employing an ultra-short pulse length laser avoids undesirable melting of the sample. Moreover, it is essential to study the optoelectronic properties of the material to perform an efficient scribe operation as each material has a different energy bandgap. A laser with a specific wavelength performs a scribe operation on a material. Initially, the material should be able to absorb that wavelength of the laser. To process a module, three scribes, P1-P2-P3, need to be done, and each scribe is done on different material. Certain materials are transparent or opaque to specific wavelengths of the laser. It is necessary to decide on the laser wavelength to be utilized to perform a certain scribe. It is done by measuring the absorbance level of the respective material with the laser. The subsequent parameter to be optimized is the scribe speed. The scribe's speed impacts the continuity of the scribe and overlap of the scribe.

Moreover, scribe speed and frequency impact the overlap of laser on the sample. The laser tool has a frequency range of 200kHz to 2Mhz. The frequency of the laser has a direct impact on the overlap. With an increasing repetition rate, the overlap level increases but reduces the pulse energy [45]. The repetition rate is maintained at a bare minimum for all the scribe patterns to have high pulse energy. The below figure 3.4 gives a schematic representation of laser surface employing a line scribe strategy to demonstrate a parameter laser pulse overlap (PO).

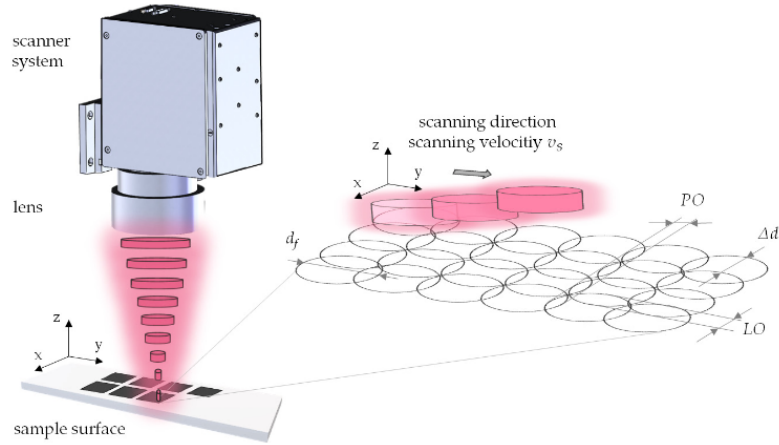


Figure 3.4: Schematic representation of laser surface employing a line scribe strategy to demonstrate a parameter laser pulse overlap (PO)[45]

Further, the ablation profile is managed with the help of varying power based on requirements. The optimization is done by performing multiple power scans to optimize the laser parameters. Ultimately, all these parameters are put together under one name, the primary quantity to be used in understanding the optimization of the laser scribe process and characterization. It is called laser fluence, i.e., the energy delivered by a laser pulse illuminating an area. This parameter varies with slight modification in any of the parameters mentioned above; it can be verified with the equation 3.2 mentioned above.

# Chapter 4

## Methodology

The experimental procedure followed for fabricating the inverted p-i-n perovskite module is mentioned in detail in this chapter. The different deposition technique implemented for depositing different layers of a perovskite mini-module is in section 4.1. An overview of perovskite module processing and characterization methods is in the section 4.2. Finally, the optimization of the laser scribing method for performing P1-P2-P3, to develop quality interconnection between cells in a module is discussed in the section 4.3 as this plays a significant role in upscaling of perovskite-based solar cells.

### 4.1 Deposition Method

To begin with, the chosen deposition techniques and their working conditions are discussed in order of layer deposition. Initially, the hole transport layer is deposited on top of commercially available ITO coated glass substrates by DC sputtering, followed by the photo-active perovskite layer deposited by the blade coating technique. Subsequently, a hole blocking, electron collecting, and a buffer layer are deposited at the stage of ETL deposition by thermal evaporation onto the perovskite stack. Finally, the thermal evaporation technique is used to deposit the metal back electrode to complete the cell architecture.

#### 4.1.1 Hole Transport Layer Deposition

A 3 X 3 (cm) commercially available ITO coated glass substrates and insulation lines on the sides was cleaned to be free from contaminants. Initially, the substrate was rinsed with the soap solution and moved to a sonicator for 10 mins. The same procedure was repeated with water, acetone, and isopropanol each for 10 minutes. Finally, the sample was dried with the help of a  $N_2$  gun.

Later, the HTL was coated on top of the ITO coating. The DC sputtering technique was used to perform the deposition of HTL, and the substrate temperature was maintained at  $24.5^\circ C$  throughout the process. The  $NiO_x$  was deposited as the HTL at low temperature. The deposited layers' thickness is around 15 nm. The overall process takes around 30 mins in total. Moreover, the  $NiO_x$  thickness was restricted mainly due to the large intrinsic resistivity of  $NiO_x$ , that increases the series resistance of the module, and

which sometimes leads to unwanted defects [46]. After the  $NiO_x$  deposition, the sample was placed in a hot chamber for annealing at  $300^\circ C$  for 20 mins for transparency.

#### 4.1.2 Perovskite Layer Deposition

The prepared double cation mixed halide perovskite solution with 5% FACl additive was deposited on top of the  $NiO_x$  by blade coating technique. The deposition was done in a blade coating chamber to avoid degradation of the sample. The solution was blade coated uniformly at a speed of 20 mm/s. In addition, the following procedure uses two dummy samples on both sides of the sample to avoid any misalignment in the thickness of deposition. The developed thickness of the photo-active perovskite layer is around 515 nm. Later, the sample was gas quenched, and this technique assisted in the up-scaling fabrication of perovskite-based solar cells [47]. Finally, the sample was annealed at  $130^\circ C$  for 30 mins.

#### 4.1.3 Electron Transport Layer Deposition

The Electron transport layer was deposited immediately on top of the perovskite layer to avoid degradation. The thermal evaporation technique was used to deposit the electron transport layer on top of the perovskite layer. As discussed in the above section 2.2.3, the ETL consists of three layers. The deposition of all three layers happens sequentially in a single run. During the process, the substrate temperature was maintained at  $24.5^\circ C$  throughout the process. Initially, the machine deposits a LiF layer of thickness of 0.8 nm. After that, the fullerene-based  $C_{60}$  was deposited, and the thickness of the mobile electron layer is 15 nm. Finally, the hole blocking layer (BCP) with a thickness of 5nm was deposited to complete the ETL stack. The processing time for depositing all three layers was 36 mins.

#### 4.1.4 Metal Back Contact Deposition

A metal back contact was deposited as a back electrode by thermal evaporation. The solid copper material was available in the form of pellets, and the number of copper pellets utilized varied on the need and thickness. The copper deposition for a mini-module was done with four pellets. Ultimately, a back electrode with a thickness of 100 nm was obtained.

## 4.2 Processing and characterization of module

Fabricating perovskite-based solar cells on a lab scale involves different deposition techniques and laser scribing techniques. All the necessary procedures are discussed individually in detail in the above sections. A course of action diagram as given in figure 4.1, helps follow the necessary steps to fabricate an inverted opaque perovskite module. Commercial ITO initially coats the cleaned soda-lime glass. Eventually, an IR laser performs a P1 scribe operation on ITO coated substrate. The P1 scribe concludes the first stage of the processing. A p-type hole transport layer was then deposited after the P1 scribe by DC sputtering, and the sample was annealed to improve the transparency.



Immediately, the perovskite active layer was blade coated inside a blade-coating closed chamber. The substrate coated with perovskite material was further gas quenched and annealed. The electron transport layer was deposited on top of the perovskite material by thermal evaporation.

Moreover, the optimized P2 parameters were used for making a P2 scribe on the perovskite stack to help the module interconnection. The above step completes the second stage of the fabrication. In the final part, the metal back contact of the module was coated by thermal evaporation. Ultimately, the performed P3 scribe completes the fabrication of a perovskite module. The module characterization was done at different stages using different equipment. The qualitative analysis was done using a SEM in EDS mode and an optical microscope, whereas the electrical performance was measured with the help of a solar simulator using 4 point probe setup. These tests are done to analyze the scribe pattern and quality of the scribe and evaluate the fabricated module's performance.

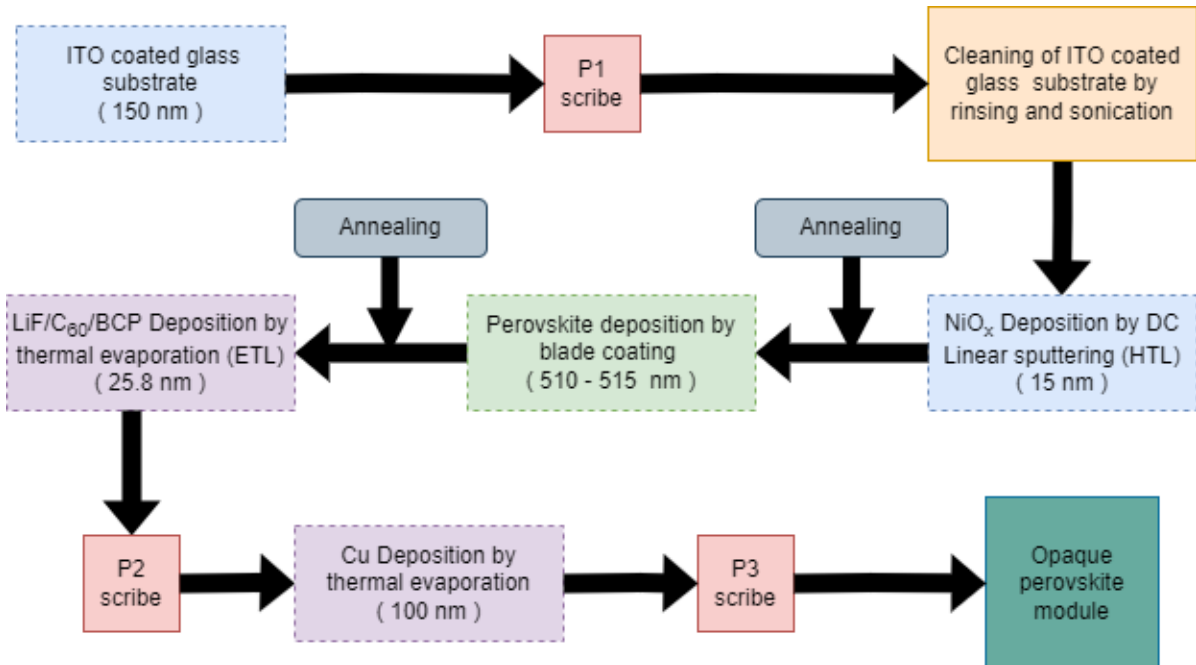


Figure 4.1: Overview of inverted opaque perovskite module fabrication

The electrical performance for cells and modules was measured with a solar simulator of class A, Sun 2000. It generates an AM1.5G spectrum. The simulator was calibrated using a reference cell with a KG3 filter to check the light intensity before measurements. Further, the module and cell measurements were performed in a glove box in an inert atmosphere to avoid damage due to humidity. A measurement head with inbuilt measurement probes and a fan keeps the device's temperature constant during illumination and measurements of single cells. The module measurement was done with a four-point probe measurement method using a Keithley 2602A. An IV sweep was done and controlled by in-house-built software. Further, the TLM measurements was done with a measuring head with the lamp turned off.

With its inbuilt EDX scan mechanism, the SEM was employed to examine the elemental composition at each scribe pattern. It was necessary to not ablate layers further than required as it affected the electrical performance by developing an undesirable shunt. In the setup, a beam of the electron was focused onto the mounted sample. The electron displaces an electron in the lower shell of an element's atom, creating an electron-hole pair. The electron from a higher energy outer shell occupied the hole created in the lower energy level of an atom. The difference in energy level between higher energy outer shell and lower energy inner shell was emitted as an X-ray. This way, the number and energy of X-rays released was estimated with the help of a spectrometer. The peaks developed at a specific energy level for each element were studied with the help of a periodic table to analyze the elemental composition at each scribe pattern. The composition was verified using both line profile and mapping technique. This way, it helped analyze the elemental composition at the scribe and control the ablation depth.

The optical microscope was used for multiple purposes. Firstly, it helped in obtaining quality images of scribe patterns. Followed by which it helped in the analysis of the depth profile. This helps in calculating the ablation depth of each scribe (P1-P2-P3). Finally, after the fabrication of the module, the scribe pattern is observed under a microscope to calculate the geometrical fill factor. The optical microscope had an added advantage with an objective focusing lens that assists in magnification. Thus, it helped in observing the damage to the sample that might lead to undesired shunts and incomplete removal of the desired layer.

## 4.3 Laser Scribing

The laser scribing technique, in general, was introduced in section 3.1. This section explains the importance of the P1-P2-P3 scribe function and its characteristics. The optimization of the laser scribing involves optimizing various laser parameters. Each parameter affects the module performance. Optimizing the P1-P2-P3 scribe, on the whole, is necessary to reduce losses for further up-scaling. So, different techniques, namely the D<sup>2</sup> method and TLM measurements, are introduced in this section.

### 4.3.1 P1 Scribe

The ITO sputtered glass substrate was taken to the glove box to perform the laser scribing operation in an inert environment. The selective ablation of the transparent conductive oxide layer (TCO) without damaging the glass substrate lying beneath is done with the help of a P1 scribe. This scribing was the first step for converting a single cell into a mini-module. Moreover, the P1 scribe helps develop electrical isolation between adjacent front electrodes of cells of a module. Initially, the laser wavelength to be used was decided to perform the scribe on a commercial ITO. The set of laser parameters to be utilized for selective ablation of ITO was optimized to obtain a quality P1 scribe. A power scan experiment was performed with a fixed wavelength and pulse length.

Initially, the frequency was kept constant, and the power and scribe speed were varied simultaneously. Later, the scribe's speed was decided based on its ability to perform a continuous scribe line with minimal damage to the layer underneath. With frequency and scribe speed set, the apparent power needed to be optimized to obtain a scribe that completely ablates ITO and develops isolation without damaging the glass. Further, to verify the electrical isolation for a point inside and outside the square scribe pattern, a qualitative analysis was performed using a multi-meter, that checked whether the scribe develops an infinite resistance between points across the scribe. It essentially helped in creating electrical isolation between adjacent front electrodes of the perovskite module.

Further, to evaluate the ablation depth and visualize the scribe pattern of the module an optical and scanning electron microscope in EDS mode was used to observe the profile of the ablated lines and to check for cracking of the glass substrate, as this might lead to undesirable effects on the electrical performance of modules by developing shunts.

### 4.3.2 D squared method

Before the ablation operation on the perovskite stack, it is necessary to understand the effect of pulse overlap and beam spot radius ( $w_o$ ) on ablation properties. So, a well-known Liu or  $D^2$  method calculates the ablation threshold fluence. The calculation is done before processing the P2 scribe to avoid damage to the underneath layers. Also, a Liu plot shows the relation between squared crater diameter and the natural logarithm of the laser pulse energy. It calculates specific parameters like ablation threshold pulse energy and the beam spot area on the sample [48].

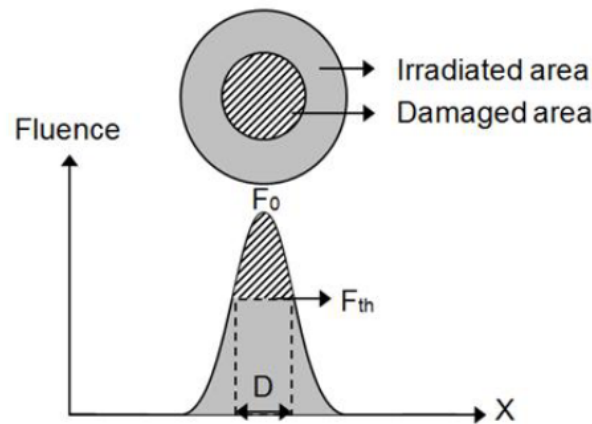


Figure 4.2: Gaussian beam profile at laser and material interaction spot [49]

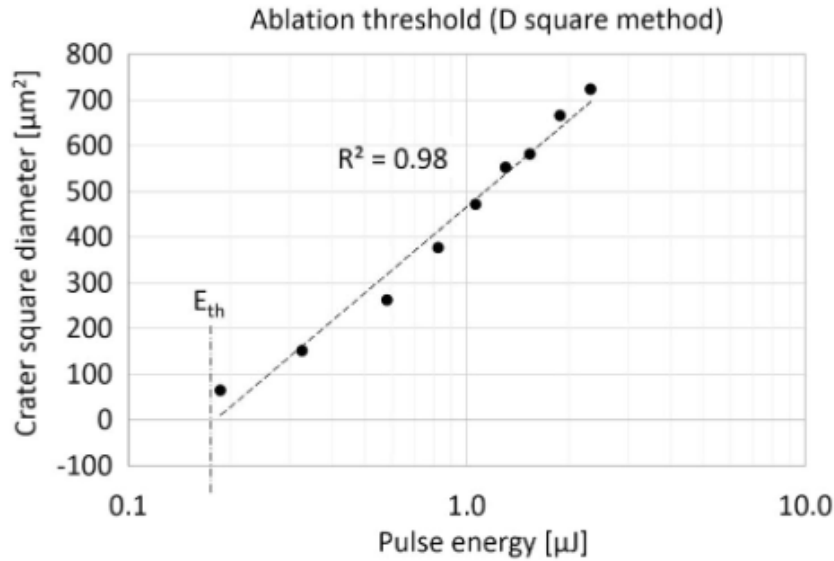


Figure 4.3: Ablation threshold fluence determination according to  $D^2$  method [50]

The ablation threshold pulse energy is the intercept at the x-axis. The ablation threshold energy is the minimum energy required to initiate the ablation of material [51]. A plot is made by gradually reducing the energy per pulse until no crater is formed on the thin-film layer. The minimum energy required to make an initial mark on the material by a laser pulse is estimated by fitting the curve. Further, the processing beam radius on the sample is calculated using the slope of the fit plot [49]. Moreover, this method calculates the pulse energy beyond which the underlying glass starts damaging the onset pulse energy. It is plotted by gradually increasing the pulse energy and measuring the crater diameter at each spot, as shown in the figure 4.3.

### 4.3.3 P2 Scribe

Optimizing the P2 scribe is pivotal in developing quality interconnection between cells in a module. Initially, the optimization was performed by determining the wavelength of the laser. The other parameters like pulse length and frequency were similar to the ones used for the P1 scribe. The two variable parameters to be optimized were the power and scribe speed. At first, the scribe speed was optimized by performing multiple scribes to check for its continuity at a specific power and to identify damage to the underneath layer.

Further, the power parameter was optimized under many conditions by performing a power scan experiment. The set power should ablate through  $NiO_x$  but avoid damaging the ITO. The optimal power was determined by calculating the ablation threshold fluence for  $NiO_x$  and ITO using the Liu method. Multiple parallel scribes were done with a range of fluences from ablation threshold fluence of ITO to higher fluences to further verify the elemental composition at the scribe pattern. The qualitative analysis was done with the help of SEM in EDS mode. It assisted in identifying the quality of the

scribe by looking for elements left behind that could affect the electrical performance of the module by developing a contact resistance between front and back contact. Further characterization was done with the help of an optical microscope to check the ablation depth of the P2 scribe at different fluence. Simultaneously, another parameter called Raster Scanning Distance was explored. The P2 scribe contains many parallel scribes to each other on a module to obtain an optimal P2 width for transferring current [42].

Finally, the P2 width was optimized to reduce inactive area loss by reducing the GFF of a module. To further verify this, a quantitative analysis was done with the help of the TLM technique. This method was used to determine the transfer length of the overall P2 scribe and to calculate the contact resistance and resistivity at the ohmic contact when scribed with lower and higher fluences. The method is further explained in section 4.3.4.

#### 4.3.4 TLM measurements

To further analyze the P2 interconnection, it is necessary to perform a quantitative analysis after the qualitative analysis. As mentioned above, the most important criteria for obtaining an optimum P2 interconnection is to remove the layer on top of the ITO to develop a direct contact between ITO and back contact (Cu). The qualitative analysis helps in picturing whether the P2 scribe is helpful in completely removing the layers above ITO or damaging ITO by employing an EDS scan and optical microscope. However, to obtain a clear picture of the Resistance at ohmic contact, a TLM measurement is needed. It helps to determine the optimal width of P2, contact resistance, sheet resistance, and resistivity [42]. The measured parameters are used to study the impact of complete or incomplete removal of layers above ITO.

Moreover, a four-probe setup is implemented to measure contact resistance. The single cell with an aperture area of  $0.13\text{cm}^2$  is used for TLM measurement. Overall, in this setup, three Resistances are included while calculating total Resistance, namely  $R_M$  Resistance of metal,  $R_{Semi}$  Resistance of semiconductor,  $R_{Sh}$  sheet resistance of ITO and  $R_{TC}$  total contact resistance. In general, the metal resistance is to be neglected while making the total resistance calculation as the resistivity of metal is significantly less when compared to  $R_{TC}$ .

$$R_T = R_{Semi} + 2R_{TC} \quad (4.1)$$

$$R_{Semi} = \frac{R_{Sh}d}{W} \quad (4.2)$$

$$R_T = \frac{R_{Sh}}{W}(d + L_T) \quad (4.3)$$

In the formula mentioned above 4.2, the parameter  $W$  is the width of the electrical contact,  $d$  is the distance between two parallelly separated electrical contacts connected by conducting film in between them and  $L_T$  the transfer length at line contact [42]. These parameters are necessary for calculating total resistance. However, the total resistance is calculated to be the sum of sheet resistance and total contact resistance between the back electrode and perovskite film as mentioned in equation 4.3. Additionally, a series of measurements is done by varying the distance between the back electrode across the cell to obtain a fit plot between the varying distance of contacts and its resistance shown in figure 4.7. Finally, the TLM measurement configuration is depicted in figure 4.4 and the arrangement for this measurement is shown in Figure 4.5 The  $L_1, L_2, \dots, L_n$  are the distance  $d$  between each line contact and it varies between each line contact. Furthermore, it helps characterize the P2 total contact resistance and ITO's sheet resistance.

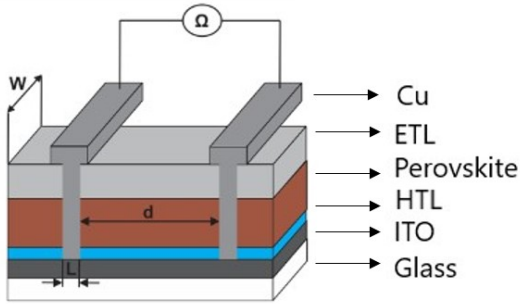


Figure 4.4: TLM Schematics used for determining P2 contact resistance and sheet resistance of ITO [52]

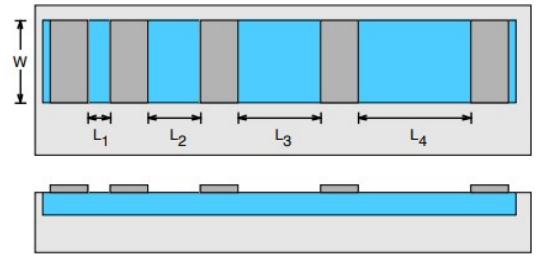


Figure 4.5: Arrangement of TLM test pattern, where blue and grey areas are film and contact respectively [53]

The metal-semiconductor interface is expressed in the form of an electrical circuit in below figure 4.6. For further optimization of device interconnection, specific contact resistivity is calculated for more precise loss analysis  $\rho_C$ . As per the current setup, the total contact resistance  $R_{TC}$  is the sum of contact resistance at the ITO/Cu interface and resistance  $R_{Cu}$  between the measurement probe and P2 contact [52]. The current flows through a semiconductor to metal back contact in the setup. However, it might experience resistance on the way through, and the current flow is also not predicted to be homogeneous over the contact region [42]. It occurs because of the quality and width of the P2 scribe [42]. The optimal transfer length for minimizing the resistance at ohmic contact is calculated with the help of the below-mentioned formula 4.5. Where  $L_T$  is the transfer length, and  $L$  is the contact length.

$$L_T = \sqrt{\frac{\rho_C}{R_{Sh}}} \quad (4.4)$$

$$R_{TC} = \frac{\sqrt{\rho_C R_{Sh}}}{W} \coth L \sqrt{\frac{R_{Sh}}{\rho_C}} + R_{Cu} \quad (4.5)$$

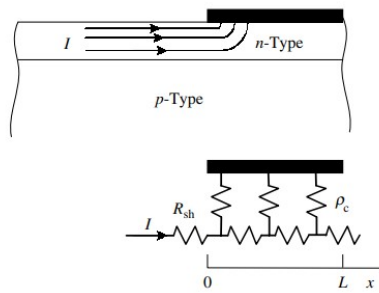


Figure 4.6: Least resistive Current transfer path between metal back contact and semiconductor [54]

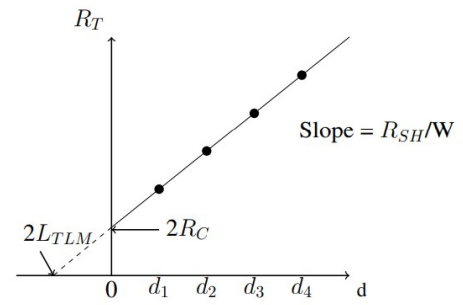


Figure 4.7: Fit plot to derive Transfer length and sheet resistance from TLM method [54]

Finally, all these data can be acquired from the plot of Total resistance against the distance between contacts. It is used to calculate the contact resistance, obtained from the point at which the curve makes an intercept at  $R_T$  after extrapolation. The following value divided by two is the contact resistance at P2 contact [54]. Moreover by extrapolating this curve, an intercept is obtained at the x-axis, which is the distance between consecutive electrodes. It provides a value of  $-2L_T$ . Further, the sheet resistance  $R_{Sh}/W$  of ITO is determined from the slope of the plot [54] and the specific contact resistivity of the metal-semiconductor interface is calculated using the above parameters. Finally, in the below chart 4.8, the processing method of a cell used to make TLM measurements is detailed.

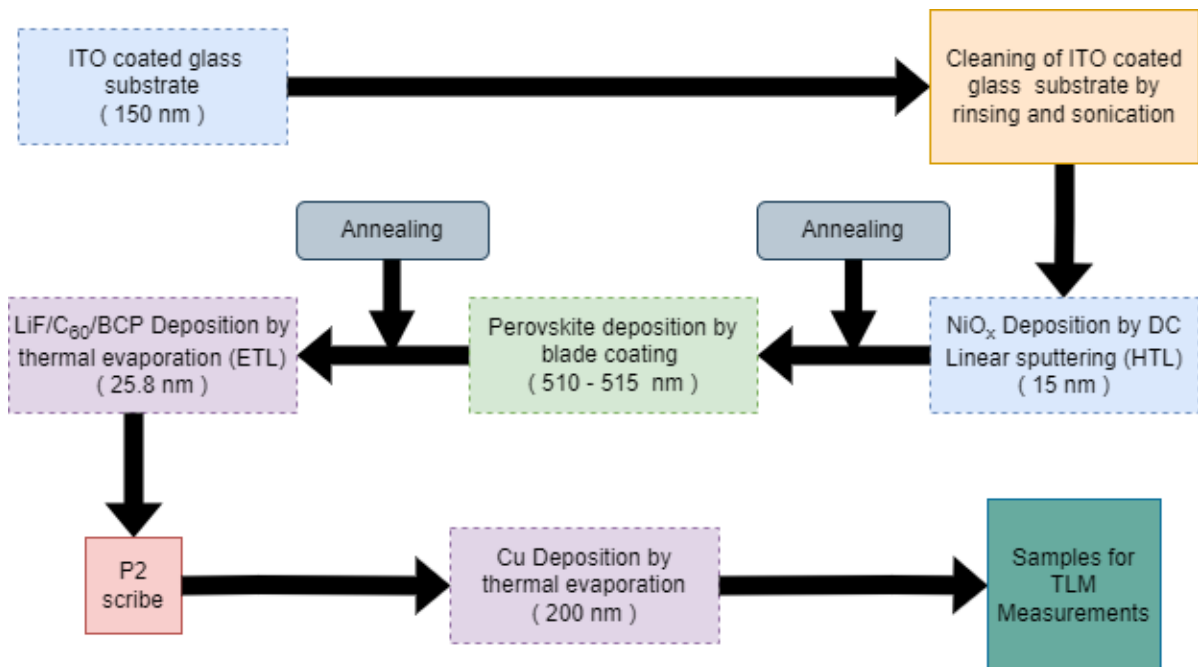


Figure 4.8: Overview of sample preparation for TLM measurements

### 4.3.5 P3 scribe

After optimizing the P1 and P2 scribe, it is necessary to optimize the P3 scribe to develop electrical insulation between two adjacent back electrodes of a cell in a module. The failure to remove the copper altogether leads to an incomplete interconnection of the module. Hence, multiple power scan tests are done before deciding on the laser parameters for the P3 scribe [42]. To further analyze the depth of the P3 scribe and the delamination phenomenon occurring underneath layers, a qualitative analysis is done with the help of a SEM in EDS mode and optical microscope to analyze the quality of the P3 scribe. Initially, the set of laser parameters, namely wavelength, pulse length, and frequency, were kept similar to once used for performing for P2 scribe. Additional parameters like stage height, scribe speed, apparent power, and spot separation were optimized simultaneously to obtain a continuous quality P3 scribe by completely ablating the Cu back electrode without interrupting the ITO.



# Chapter 5

## Results and Discussions

The results of this research work are reported in this chapter. First, the optimized laser parameters for the P1, P2, and P3 scribes are discussed in different sections. Finally, the effects of upscaling and the drop in electrical performance of modules when upscaled are discussed.

### 5.1 P1 scribe

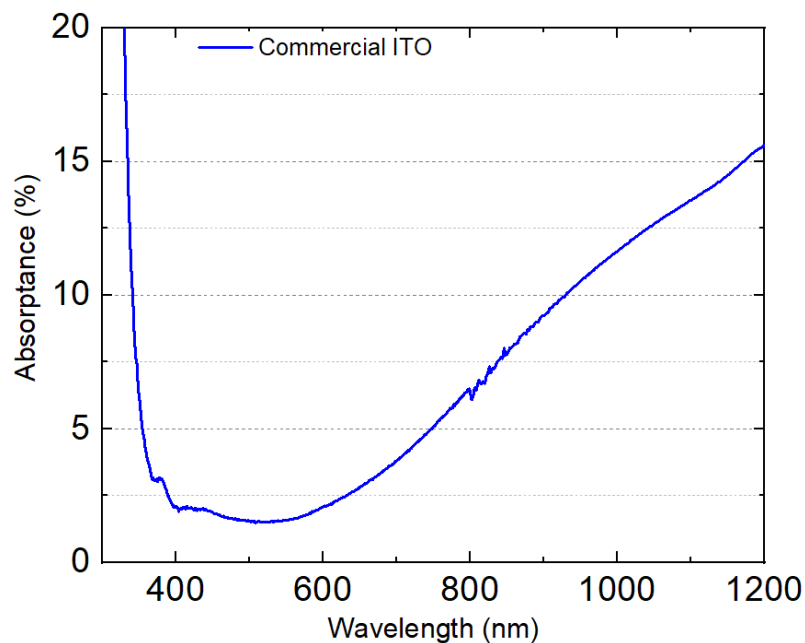


Figure 5.1: Absorptance spectrum of the commercial ITO

The P1 scribe was performed with the help of an IR laser. It was decided based on the absorptance of commercial ITO at the respective wavelength. The absorptance spectrum in figure 5.1 was used in finding the optimal laser wavelength for the P1 scribe. Initially, the stage height of the laser tool was adjusted to a height of -73.02 mm from the chuck to focus the IR laser on the substrate. The frequency of the laser was set at 200khz.

The P1 scribe laser parameters could isolate the front electrode. However, it needs to be further optimized to reduce the inactive area losses. As discussed, the most critical objective of the P1 scribe is to isolate the front electrode of one cell from another of a module. The two most critical parameters are needed to be further optimized are power and scribe speed; it was done following the power scan experiment. The power scan was performed between an apparent power of 230 MCS and 290 MCS in steps of 10 MCS. The MCS represents 0.1% of the maximum power of laser. Simultaneously, the scribe speed was altered from 100 to 500 mm/s in steps of 100 mm/s. The scribes were made in a square pattern to perform an electrical test with the help of a multi-meter. The multi-meter was used to check conductivity between the entire length of the square pattern to determine the resistivity at each scribe. The test was done with the sensitivity of a multi-meter set at 200k ohms per volt. The conduction test results are in the below table 5.1. Moreover, one of the insulating parameters was used as the final parameter for the P1 scribe. This decision was made by performing a qualitative analysis where the scribe's continuity, ablation depth, the width and the elemental composition were observed.

Power (MCS) / Speed (mm/s)	100	200	300	400	500
230 (0.817 W)	Conductive	Conductive	Conductive	Conductive	Conductive
240 (0.922 W)	Conductive	Conductive	Conductive	Conductive	Conductive
250 (1.032 W)	Insulating	Insulating	Conductive	Conductive	Conductive
260 (1.151 W)	Insulating	Insulating	Insulating	Conductive	Conductive
270 (1.278 W)	Insulating	Insulating	Insulating	Conductive	Conductive
280 (1.410 W)	Insulating	Insulating	Insulating	Conductive	Conductive
290 (1.548 W)	Insulating	Insulating	Insulating	Insulating	Conductive

Table 5.1: Insulation test for scribes of power scan experiment

First, the power parameter was decided based on the ability to isolate. There was no thermal stress on the edges for all the power above 230 MCS and below 290 MCS, and the ablation depth was not beyond 150 nm. So it is safer to use power within this range without causing cracks on the scribe's edges that might affect the active area. Following that, the scribe speed was optimized with the power scan technique. The scribes done at higher speed leads to significant gaps between each scribe spot, which fails to isolate the scribe. As we can see in the above table for scribe speed 400 and above, the P1 scribe fails to isolate the front electrode of one cell to another. Whereas at slower scribe speed, it is possible to achieve continuous scribe with scribe spots overlapping one another. However, it leads to an increase in the width of the scribe and an increase in overlap percentage. It results in deeper ablation at scribe spots. So it is necessary to strike a balance between overlap percentage and scribe width when optimizing the scribe speed.

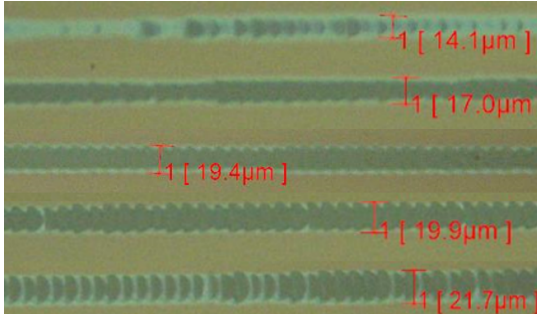


Figure 5.2: A series of parallel P1 scribes at power 260 MCS and at scribe speeds from 100 mm/s at bottom to 500 mm/s at top

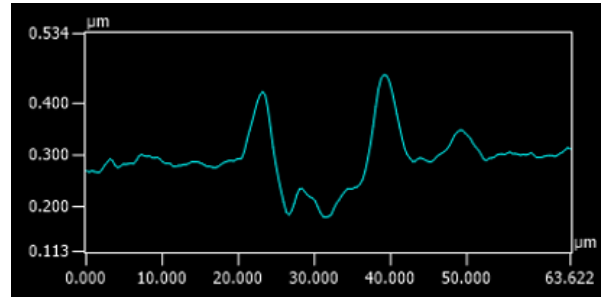


Figure 5.3: Microscopic image of ablation depth when scribed at 260 MCS and 300 mm/s for P1 scribe

A power scan was performed with a power of 260 MCS and scribe speed from 100 mm/s to 500 m/s from bottom to top. There was no insulation at higher speeds of 400 mm/s and 500 m/s, so this was disregarded. At a lower speed of 100 mm/s, the scribe's width is  $21.7 \mu\text{m}$ , and the ablation depth was beyond 150 nm at some spots due to an increase in the overlap. The optical microscope at 25x magnification was used for width and profile measurements. Among the other two scribe speeds, they both resulted in a continuous scribe, but the width of the scribe at 300 mm/s is a bit smaller. So it is optimal to scribe at power 260 MCS and speed 300 mm/s to improve the geometrical fill factor where the scribe width is around  $19.4 \mu\text{m}$ . This is shown in the above figure 5.2.

To further confirm the ablation quality at this parameter, a SEM imaging at 3.6kx magnification was done to observe any stress or crack at the edges of the scribe. The scribe at power 260 MCS and speed 300 mm/s had no external stress. Further, elemental analysis was done using SEM in EDS mode. A line scan and mapping method was used to observe the elemental composition scribe. The results prove negligible damage to the layer underneath with high Na counts and low In and Sn count. The line scan and mapping in the figure 5.4 and 5.6, shows that the scribe has removed the ITO at the scribe without damaging the glass underneath. The white line in figure 5.4 denotes the scribe spot. The selective removal of elements for scribes at power 260 MCS and speed 300 mm/s, successfully isolates the front electrode of one cell from another in a module.

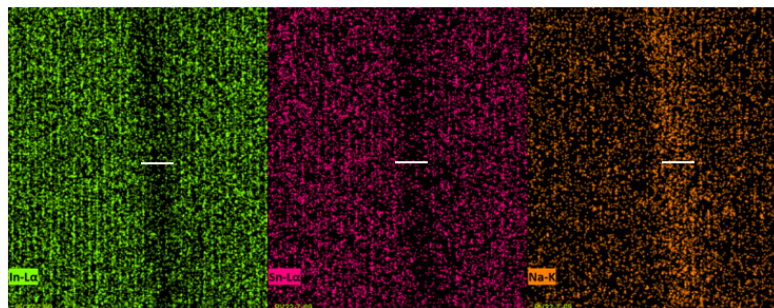


Figure 5.4: Elemental composition of the P1 scribe at power 260 MCS and scribe speed 300 mm/s using EDS scan

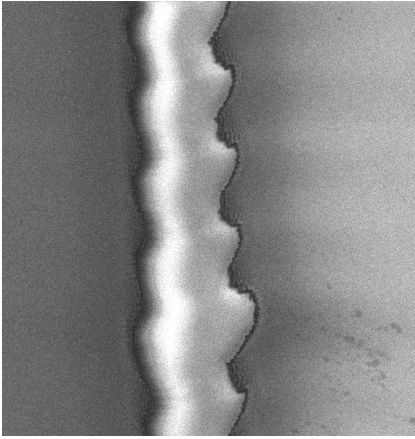


Figure 5.5: SEM image at 3600x magnification for P1 scribe at power 260 MCS and scribe speed 300 mm/s

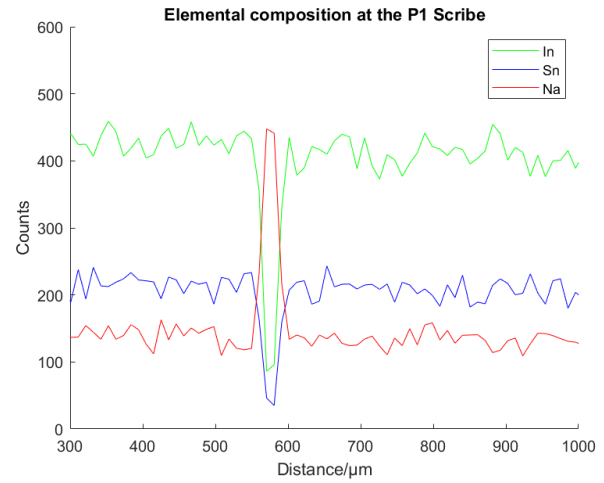


Figure 5.6: Elemental composition of the P1 scribe at power 260 MCS and scribe speed 300 mm/s using EDS scan

## 5.2 P2 scribe

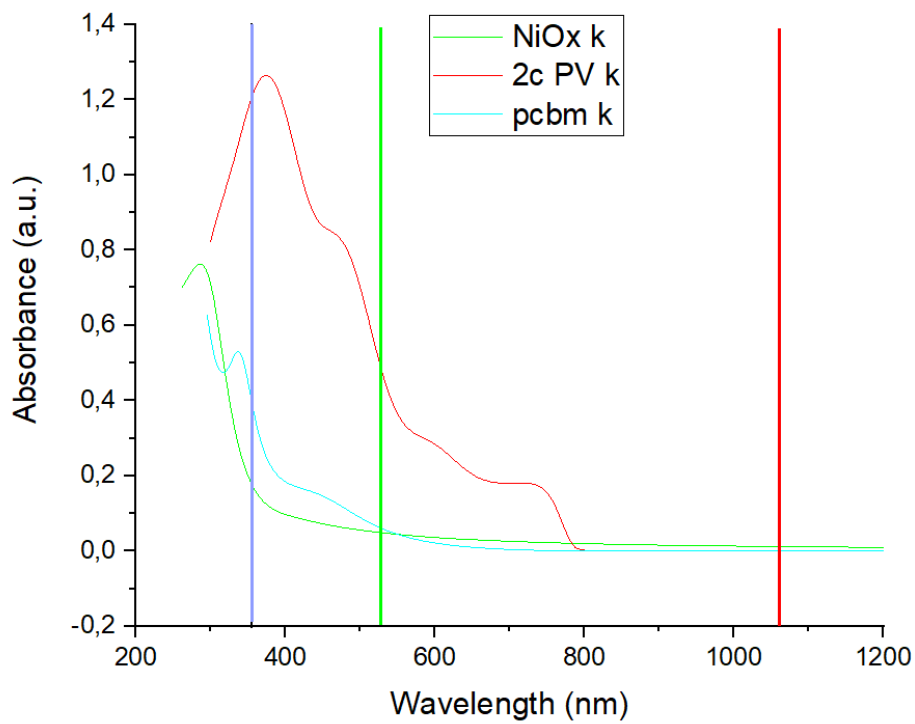


Figure 5.7: Absorbance spectrum of the perovskite cell architecture

The P2 scribe was performed with the help of a UV laser. Based on the absorbance of the double cation perovskite from the absorbance spectrum figure 5.7. The stage height of the laser tool was adjusted to -67.00 mm from the chuck to focus the UV laser on the substrate. The frequency of the UV laser and the scribe speed was set at 250 kHz and 200 mm/s respectively for all the below experiments on P2 scribe. For the respective scribe speed, the scribes are continuous and it is further confirmed with experiments done for P3 scribe in section 5.3. The next parameter, power should be optimized to ablate through the ETL, perovskite layer, and HTL but avoid damaging the ITO. The optimal power was determined by calculating the ablation threshold fluence for  $NiO_x$  and ITO with the perovskite stack. The following procedure was done by making spots with apparent power from 230 MCS to 320 MCS in steps of 10 MCS with high spot separation to isolate.

Further, the crater diameter of the ablated  $NiO_x$  spot was measured with the help of an optical microscope for each power to make a plot of pulse energy vs crater diameter. This way, the ablation threshold of  $NiO_x$  was calculated with a fitted curve. As per the  $D^2$  method, the Gaussian beam profile is related to the fluence, and the slope of the fit plot gives the diameter of the focal plane  $2w_o$  [49]. The calculated parameters are in table 5.2. Finally, the ablation threshold of  $NiO_x$  is determined to be  $14 \text{ mJ/cm}^2$  by the intercept of the fit curve from the plot 5.8. Further, the point at which the ITO starts cracking is determined similarly. This point is the onset pulse energy, where the  $NiO_x$  is completely removed, and ITO ablation starts. As per research, this point is the optimal fluence for P2 ablation [42]. The ablation threshold fluence of ITO with the respective perovskite stack was calculated to be  $110 \text{ mJ/cm}^2$  from the plot 5.9. The corresponding apparent power to this fluence is 244 MCS. It was calculated using the abovementioned formula in section 3.2.1.

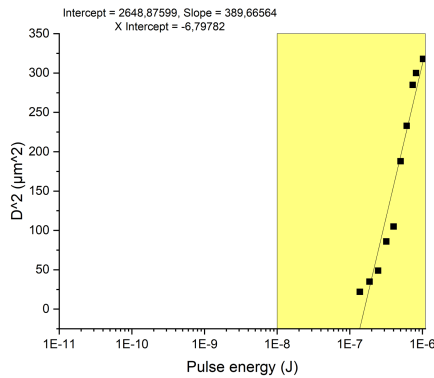


Figure 5.8:  $D^2$  of ablated spot in  $\mu\text{m}^2$  vs pulse energy (J) for determination of  $NiO_x$  ablation threshold fluence

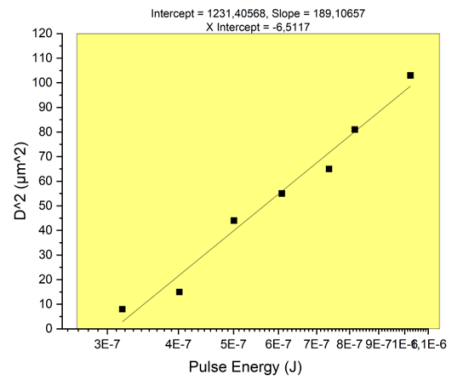


Figure 5.9:  $D^2$  of ablated spot in  $\mu\text{m}^2$  vs pulse energy (J) for determination of ITO ablation threshold fluence

Parameters	NiOx	ITO
Beam Spot (W) ( $\mu\text{m}^2$ )	13.9	9.72
Diameter of Spot (D)( $\mu\text{m}^2$ )	27.91	19.44
Area of Spot ( $\text{cm}^2$ )	$6.11 \cdot 10^{-6}$	$2.96 \cdot 10^{-6}$
Ablation Threshold ( $\text{mJ}/\text{cm}^2$ )	14	110

Table 5.2: Ablation Threshold fluence parameters for  $\text{NiO}_x$  and ITO layers ablated with UV laser

A qualitative analysis was performed to further verify the power parameter by doing a power scan experiment with a constant scribe speed of 200 mm/s. Optical microscopic imaging was done for parallel scribes with increasing power from ITO ablation threshold fluence to higher fluence to observe the ablation of ITO. In the below figure 5.10, it can be observed that the ITO ablation increases at higher power. At the center of scribes, it pictures the ITO damage and ablation of the underneath layer at higher fluence. It is due to the Gaussian profile of the laser.

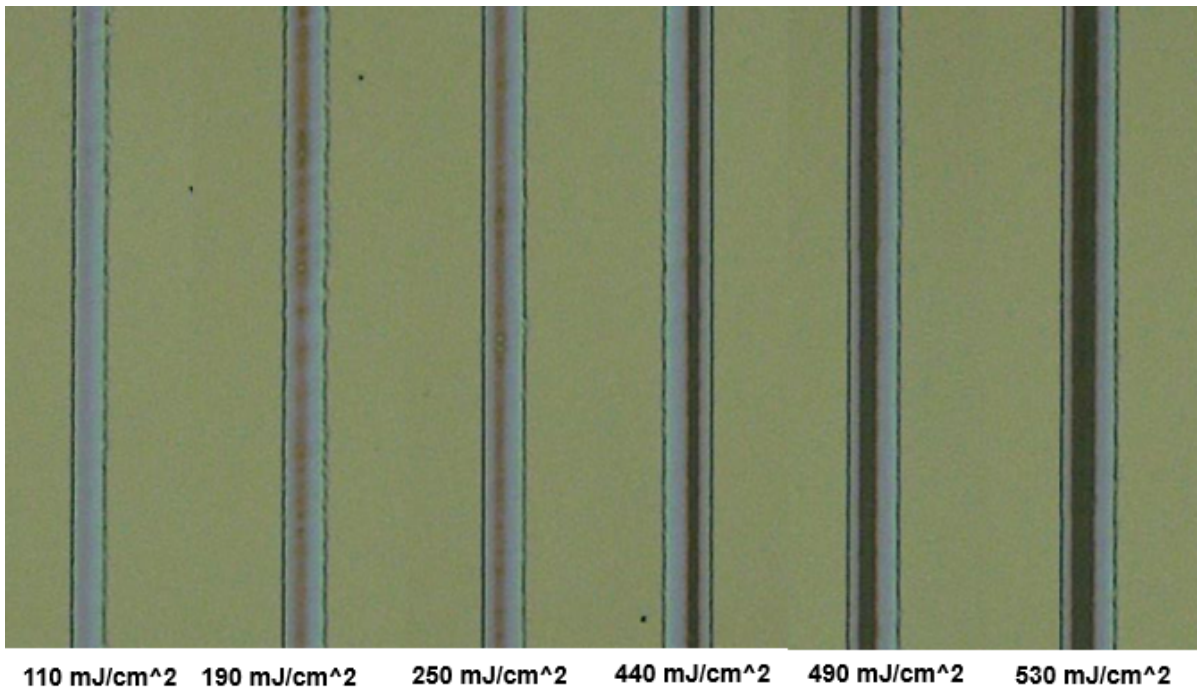


Figure 5.10: Parallel scribes for power scan experiment with increasing fluence from left to right



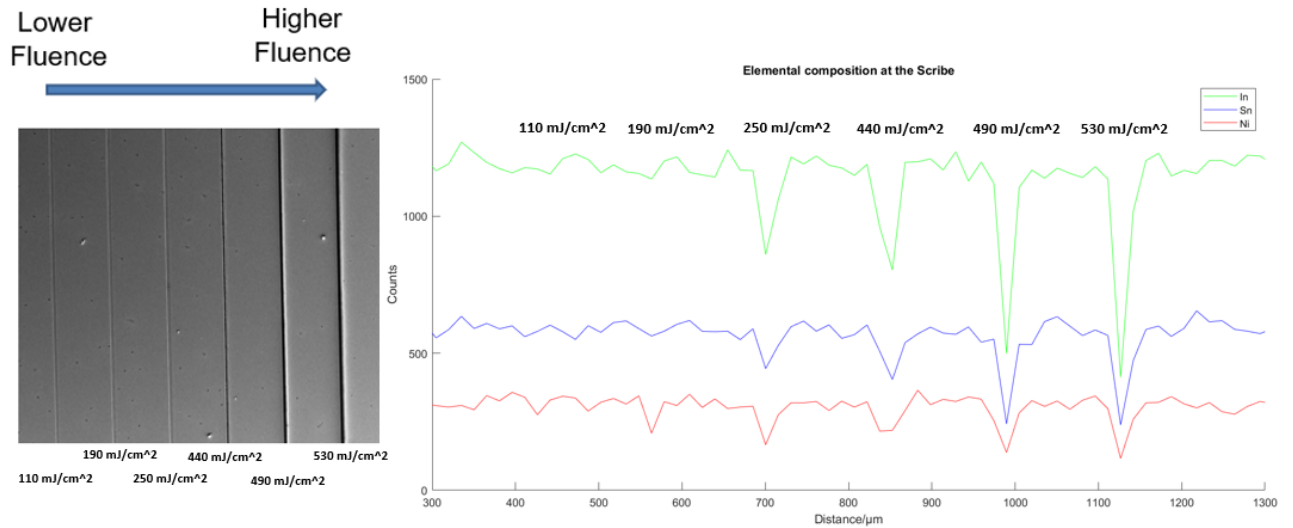


Figure 5.11: Elemental composition at each scribe under SEM in EDS mode

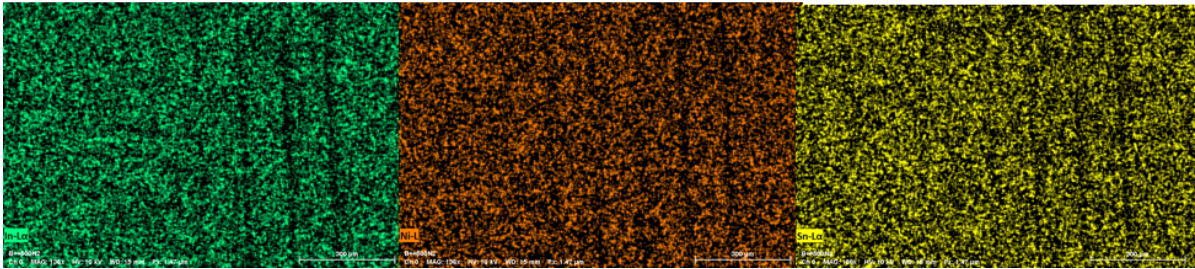


Figure 5.12: Elemental composition at each scribe under mapping mode

The main objective of the P2 scribe is to ablate all the layers between the front and back contact to minimize contact resistance and develop a quality interconnection for cells in a module. So SEM analysis in EDS mode was performed to verify the elemental composition at each scribe pattern. In the above figure 5.11, the Ni count was observed at each scribe. The main objective is to ablate  $NiO_x$ , ultimately to reduce contact resistance at ohmic contact. It was done by comparing the Ni count at ablation threshold fluence and higher fluence. The EDS scan shows that the Ni count reduces while moving to higher fluences, and the Ni count is lowest at higher fluence compared to ablation threshold fluence. However, there is also ITO damage at higher fluence and no ITO damage at ablation threshold fluence. To further verify, the electrical performance of modules was tested at ablation fluence and higher fluence to analyze the effect of Ni left behind and to identify the fluence beyond which the module performance drops.

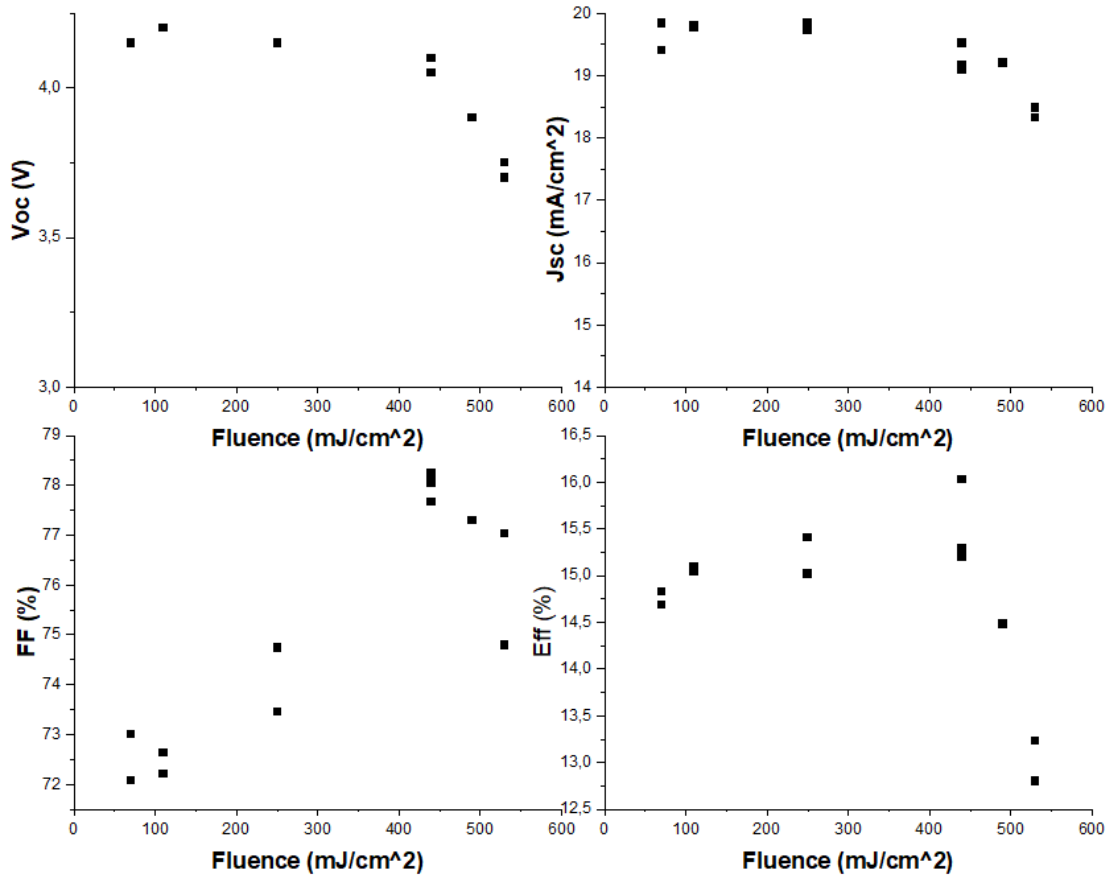


Figure 5.13: Electrical performance of modules with P2 scribes at different fluences

The interconnection quality is verified with the help of the Fill Factor of modules [42]. A batch of samples with increasing fluences for P2 scribes with a constant width of  $110 \mu\text{m}$  was measured to analyze the electrical performance. In analyzing the above figure 5.13, the fill factor of the module increased with increasing fluence. It attests to the findings from EDX analysis and shows the effect of  $\text{NiO}_x$  left behind at scribe spots. It shows that the ablation threshold fluence of ITO is not the optimal fluence for P2 ablation.

Moreover, from the above figure 5.13, at a fluence of  $440 \text{mJ}/\text{cm}^2$ , the fill factor of the module was found to be the highest. It is due to the complete removal of  $\text{NiO}_x$ , verified with the EDS scan. However, when analyzing the EDS scan for parallel scribes, the Ni count at fluences above  $440 \text{mJ}/\text{cm}^2$  for P2 scribe is lower than for scribes at  $440 \text{mJ}/\text{cm}^2$ . However, at higher fluence above  $440 \text{mJ}/\text{cm}^2$ , there is a drop in the module's fill factor and voltage. The fill factor and voltage drop can be due to the development of shunts at higher fluence. The shunts can be due to the cracks at the adjacent layer, complete removal of ITO, or cracking of glass substrate underneath. The JV plot for all the above modules are in appendix A.2. Further, optimization of the P2 scribe is done at fluence  $110 \text{mJ}/\text{cm}^2$ , the ablation threshold fluence of ITO, and at  $440 \text{mJ}/\text{cm}^2$ , where the module performs at its best.



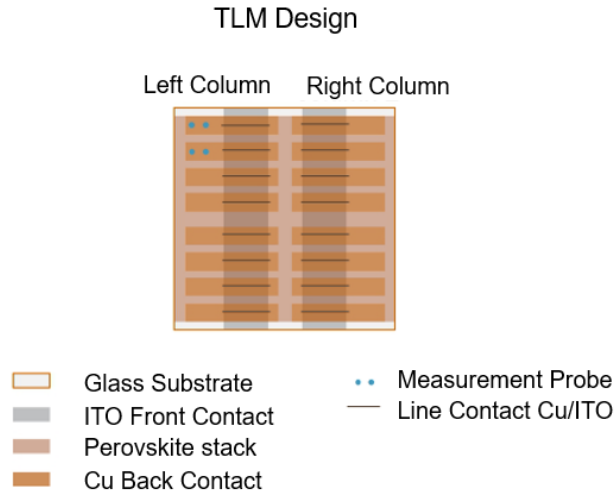


Figure 5.14: Design of TLM devices used for line contact P2 interconnection [52]

The TLM measurement was done for different fluence at different contact length. The TLM processing and measuring technique are discussed in the chapter 4.3.4. The probes measure the total resistance between line contacts at different distances. Each line contact was scribed at an equal distance apart from each other. Later, Cu is coated on top of the line contact with a thickness of 200nm. The increased copper thickness was to reduce the resistance due to metal contact. In the below graph 5.15, the total resistance for scribes at  $110\text{ mJ/cm}^2$  fluence and different contact length is measured at different distances along the cell. The contact length is varied from one measurement to another by making parallel scribes at RSD 10  $\mu\text{m}$  to obtain different contact length. The same measurement is done for cells at fluence  $440\text{ mJ/cm}^2$ . It is shown in the below graph 5.16. The TLM plot was used to calculate the total contact resistance, resistivity, sheet resistance, and transfer length for P2 scribes performed at different fluences and P2 widths. It helped study the impact of contact resistance at ohmic contact and optimize the P2 width. The calculated parameters are in the appendix A.

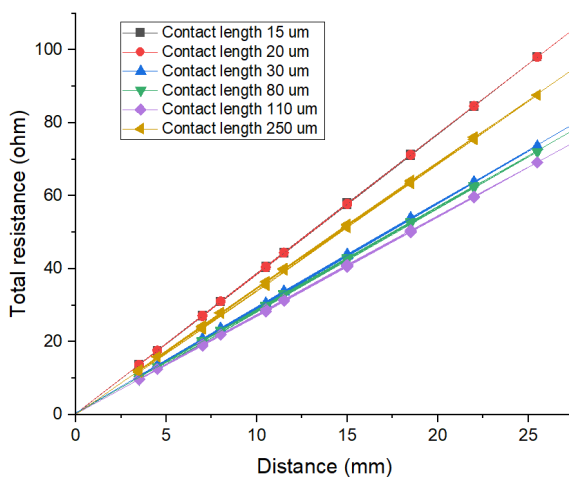


Figure 5.15: Transmission line measurement at lower fluence  $110\text{ mJ/cm}^2$

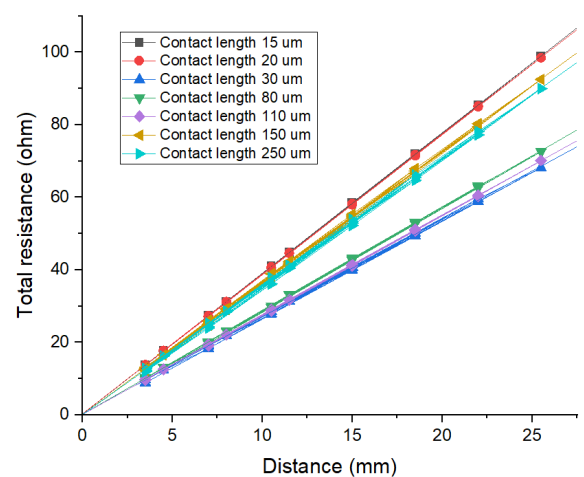


Figure 5.16: Transmission line measurement at higher fluence  $440\text{ mJ/cm}^2$

The contact resistance and resistivity from the below plots are used to find the optimal fluence and P2 width. The below graph 5.17, shows that the contact resistance drops at higher fluence, which further attests to the findings from the EDS scan and module measurements. It shows the impact of  $NiO_x$  left behind at the ohmic contact. The below figure 5.17, shows that the contact resistance drops for all the fluences at broader contact lengths and saturates beyond a certain point. However, a wider contact length can reduce the increasing contact resistivity and contact resistance, but a wider contact length will also reduce the geometrical Fill Factor of the module. So, after a certain width, it is over dimensioning of P2 width. So it is necessary to obtain the optimal transfer length for the particular P2 scribe.

Another important observation from the plot is that at lower P2 width below  $30\mu m$ , the contact resistance at line contact drops drastically and happens at all the fluences. To analyze the drop in contact resistance at lower P2 width, the scribe profiles were analyzed, and a batch of modules was prepared at smaller P2 width to analyze the electrical performance and to verify the possibility of the module working at a smaller contact length as this could further increase the GFF.

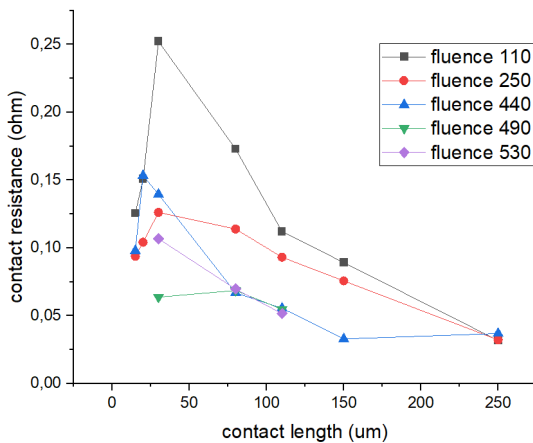


Figure 5.17: Plot of Contact Resistance against contact length at different fluences

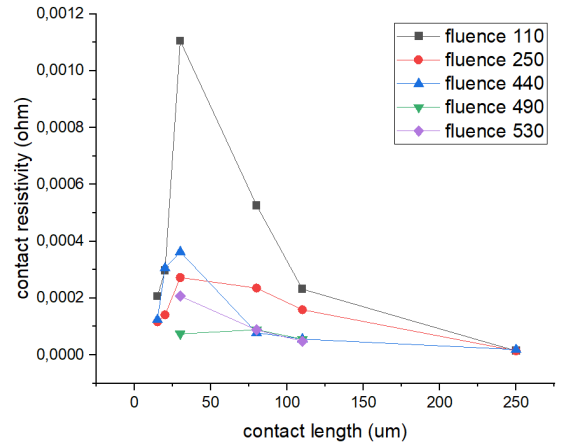


Figure 5.18: Plot of Contact resistivity against contact length at different fluences

As discussed above, it is optimal to have a P2 width less than or equal to  $L_T$ . The transfer length plot of the respective P2 scribes at fluences  $110mJ/cm^2$  and  $440mJ/cm^2$  is shown in figure 5.20. The figure shows that the transfer length is high for lower fluences and low for higher fluences. It is due to the presence of  $NiO_x$  that the transfer length increases when scribed with lower fluence. The transfer length range for both the fluences is obtained by calculating the average and standard deviation of the transfer length at different contact lengths from the table A.1. At a fluence of  $110mJ/cm^2$ , the transfer length ranges between  $26\mu m - 65\mu m$ . Whereas for a fluence of  $440mJ/cm^2$ , the transfer length is between  $13\mu m - 38\mu m$ .

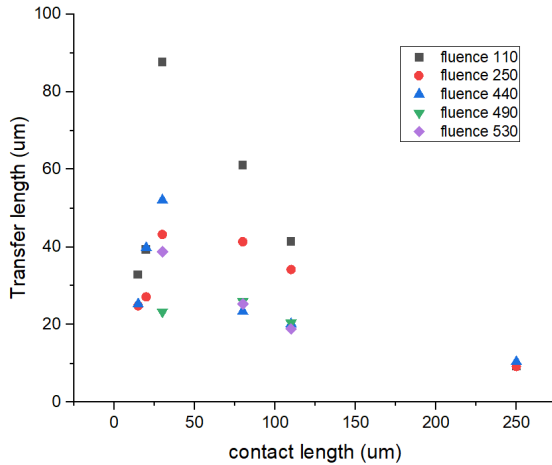


Figure 5.19: Plot of transfer length against contact length at different fluences

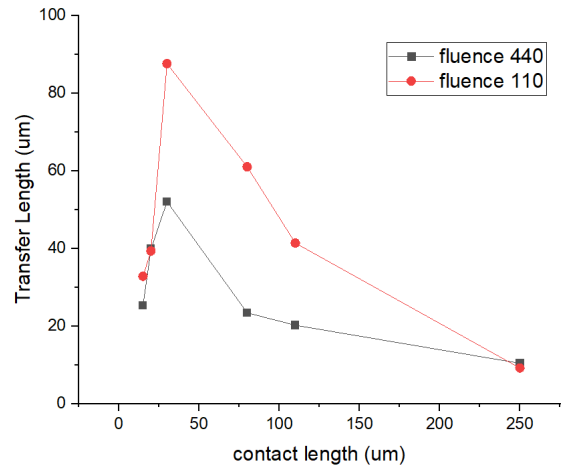


Figure 5.20: Plot of transfer length against contact length at fluences  $110mJ/cm^2$  and  $440mJ/cm^2$

Further, to finalize the transfer length, a set of modules was prepared with two fluences  $110mJ/cm^2$  and  $440mJ/cm^2$  and with different P2 widths. The electrical performance of the respective modules is in figure 5.21. It was done to obtain the transfer length and to understand and optimize the module performance at different contact lengths for both the fluence.

The module performance at both the fluences at different P2 width is shown in plot 5.21. The test results show that at higher fluence, the fill factor saturates for all the modules from a P2 width of  $30\mu m$ . It shows that a quality interconnection is reached at a width of  $30\mu m$ . Whereas for lower fluences, the fill factor was lower than for higher fluence at all P2 widths, and the fill factor did not saturate as it did with higher fluence. It shows that a higher P2 width is required at lower fluence to reduce the contact resistivity at ohmic contact. So that modules could perform efficiently with minimal interconnection losses. However, if done, so it reduces the geometrical fill factor. Another observation which explains the happening in figure 5.17, from the earlier TLM results, it was observed that the contact resistance was low for scribes at lower P2 width  $15\mu m$  and  $20\mu m$ . As per the results, it should be the optimal width as it increases the GFF and reduces contact resistance. However, it contradicts the results in figure 5.21, at lower P2 width below transfer length, there is a current crowding phenomenon that occurs [54]. The current crowding phenomenon restricts the flow of charges at ohmic contact and reduces the fill factor of the module. So to avoid this, it is necessary to have a P2 width above transfer length. So, the P2 scribe is done with a fluence of  $440 mJ/cm^2$  and width  $30\mu m$ . As per the above results, this is the optimal P2 to proceed forward. The other optimized parameters of P2 scribe are shown in table 5.3 and 5.4. Finally, The JV plot for all the above modules are in appendix A.3 and A.4.

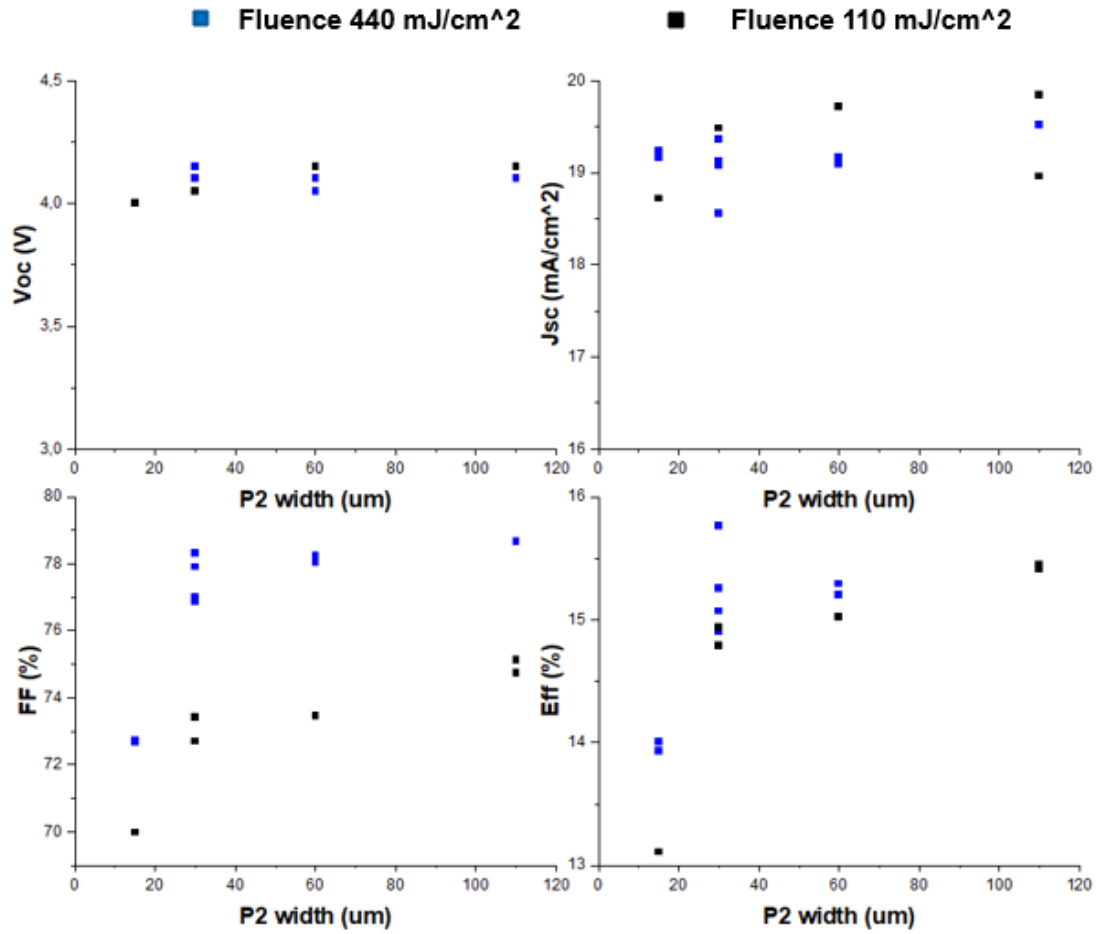


Figure 5.21: Module performance at different P2 width for fluence  $110 \text{ mJ/cm}^2$  and  $440 \text{ mJ/cm}^2$

The P2 scribe with a width of  $30 \mu\text{m}$  was performed by making two scribes lines using the above parameter. The two scribes are done at  $10 \mu\text{m}$  distance apart. This distance is called the raster scanning distance. It was done to avoid overlap between two scribes that causes further ablation and stress at ITO. The below figure 5.22 shows the scribe spot and scribe line with optimized P2 parameters. The ablation of the ITO layer can be seen in the figures in the form of depth profiling using an optical microscope, and it occurs at the center of the laser beam, down to the Gaussian profile of the laser beam. Finally, the ablation depth of the P2 scribe was measured to be around  $580 - 600\text{nm}$ . It shows that it ablates the perovskite layer,  $\text{NiO}_x$  and a bit of ITO. Similarly, an optical microscope width investigation was done for P2 scribes at fluence  $440 \text{ mJ/cm}^2$  and different widths.

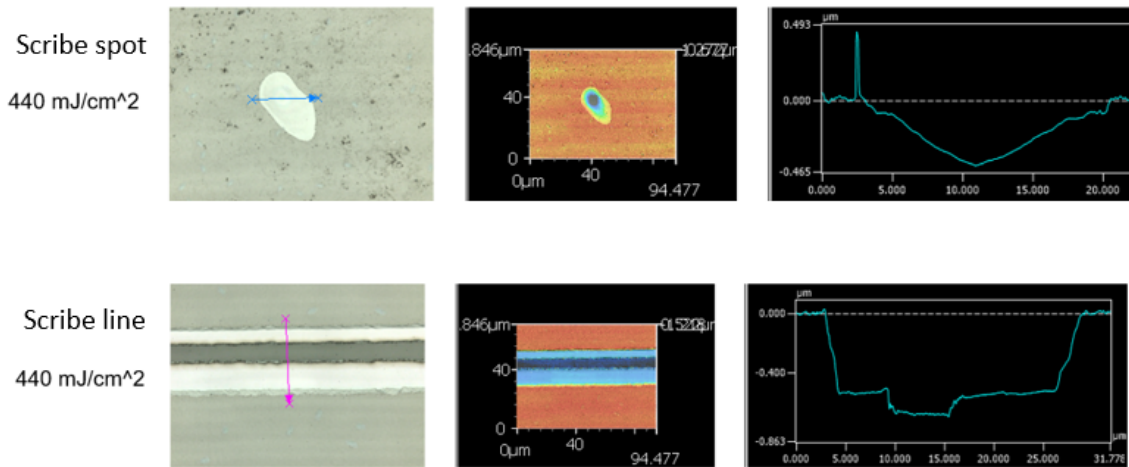


Figure 5.22: Depth profiling of P2 scribe spot and scribe line under optical microscope

### 5.3 P3 scribe

The P3 scribe was optimized to avoid discontinuity in the scribe line as that leads to incomplete isolation of back electrodes and to reduce the width of the P3 scribe as that could impact the inactive area losses. To avoid this, a power scan experiment was done to optimize the P3 scribe.

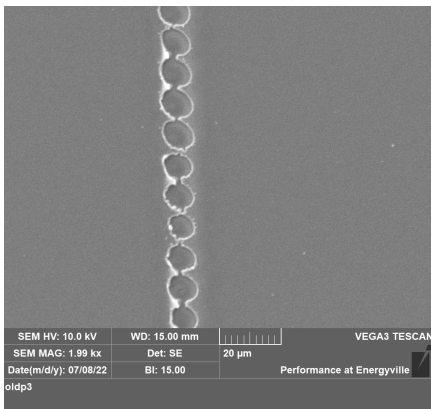


Figure 5.23: P3 scribe before optimization under SEM

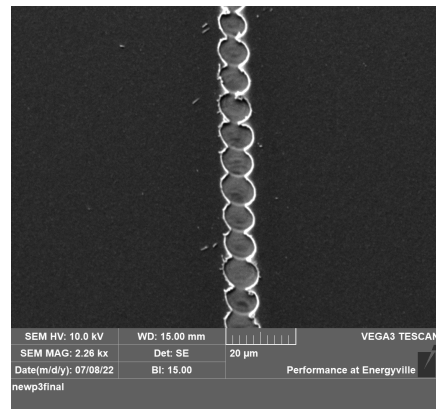


Figure 5.24: P3 scribe after optimization under SEM

Similar to the P2 scribe, the UV laser was used to perform the P3 scribe. Initially, the stage height of the laser tool was adjusted to a height of -66.72 mm from the chuck, to focus the UV laser on the substrate. The laser frequency was set at 250 kHz, similar to the P2 scribe. The most critical objective of the P3 scribe is to isolate the back electrode of one cell from another of a module. Further, the power scan experiment was performed to optimize the power and scribe speed parameters. The power scan was performed between an apparent power of 210 MCS and 320 MCS in steps of 10 MCS with a fixed spot separation of  $10\mu\text{m}$  and scribe speed of  $500\text{mm/s}$  as shown in the below figure 5.25.

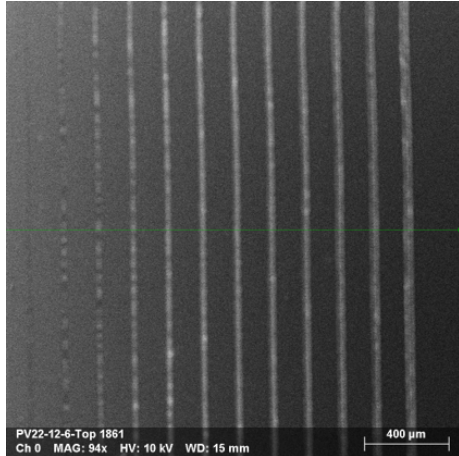


Figure 5.25: Parallel scribes at power from 210 MCS to 320 MCS under SEM

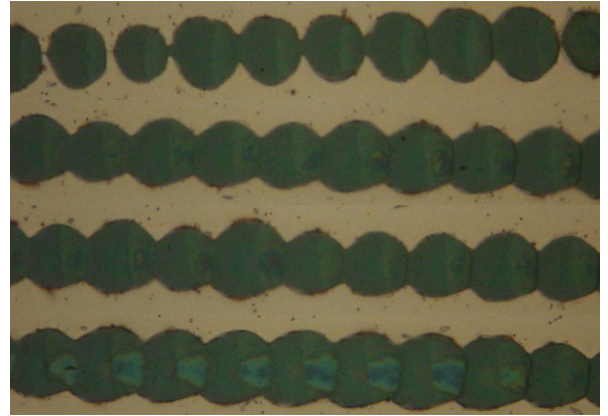


Figure 5.26: P3 scribes at different power from 250 MCS at top to 280 MCS at bottom under optical microscope

The scribe lines at the power of 270 MCS and 280 MCS were continuous, and there was no copper left behind at the scribe lines. At a power of 250 MCS, the scribe spots were not overlapping, making the ablation discontinuous and incomplete. Moreover, at a power of 280 MCS, the ablation depth is much more visible in the form of little blue spots at overlaps that show the ablation of ITO underneath. This is harmful and will lead down the module performance by developing shunts. The further optimization of scribe speed and pulse overlap is carried forward with the power of 270 MCS.

From P2 optimization observations, the scribe speeds were tested from 200 - 500 mm/s for P3. The scribes at 200 mm/s were continuous and ablated the copper entirely without damaging the ITO. Finally, the spot separation was optimized to make it thin and continuous and also ensure complete copper removal at each scribe spot. The spot separation of the laser beam was set at  $8\mu\text{m}$ . To further verify the ablation quality and confirm the complete ablation of Cu, an EDS scan was done for qualitative analysis. It is shown in the below figure 5.27. The EDS scan results show that at the scribe spot, the Cu was removed entirely. Whereas the upward trend of Pb, Cs, In, and Sn counts show that the scribe has not removed the perovskite layer and ITO, this parameter can be used for the P3 scribe. The final P3 scribe has a thickness of around  $11\mu\text{m}$ .



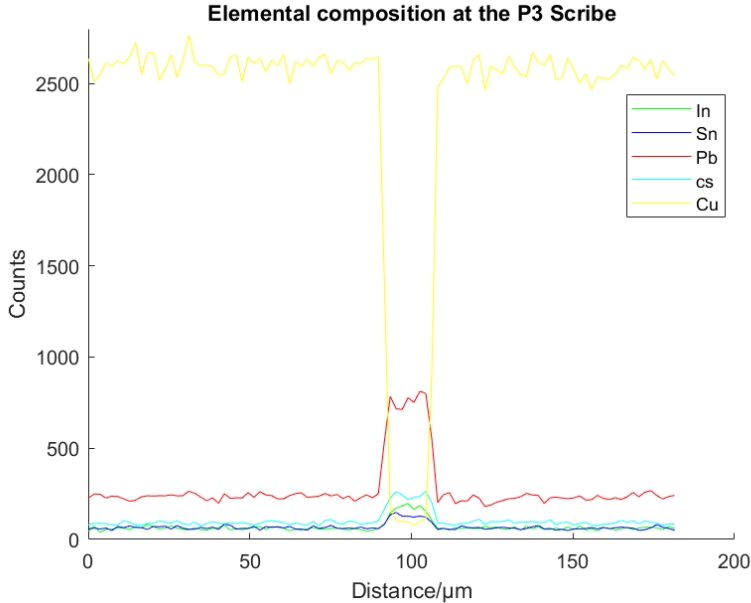


Figure 5.27: Elemental composition of P3 scribe under SEM in EDS mode

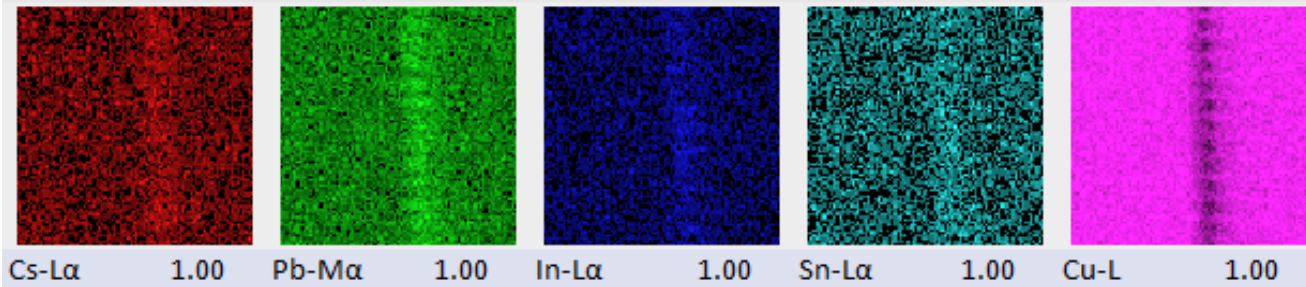


Figure 5.28: Elemental composition of P3 scribe under SEM in EDS mode

## 5.4 Overview of laser parameters

In the below table 5.3, the chosen optimal laser parameters of each scribe are mentioned. These parameters were used to make the laser scribes on the module. Further, the losses in up-scaling from cell to module are reported and analyzed.

Scribe	Wavelength	Frequency	Power	Stage Height	Scribe Speed	Spot Separation
unit	nm	kHz	MCS	mm	mm/s	mm
P1	1064	200	260	-73.02	300	0.0100
P2	355	250	290	-66.72	200	0.0100
P3	355	250	270	-66.72	200	0.0080

Table 5.3: Laser parameters of each scribe line

P2 scribe parameters	Values
P2 width ( $\mu\text{m}$ )	30
Raster scanning distance ( $\mu\text{m}$ )	10
Laser Fluence ( $\text{mJ}/\text{cm}^2$ )	440
Scribe spot diameter ( $\mu\text{m}$ )	15
Ablation depth (nm)	590

Table 5.4: Optimized parameters of P2 scribe

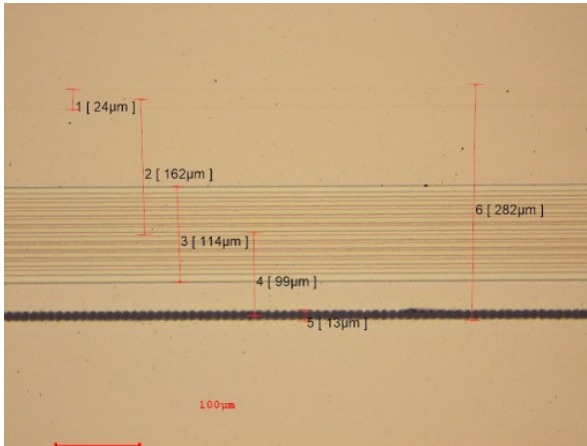


Figure 5.29: The scribe design before laser parameter optimization

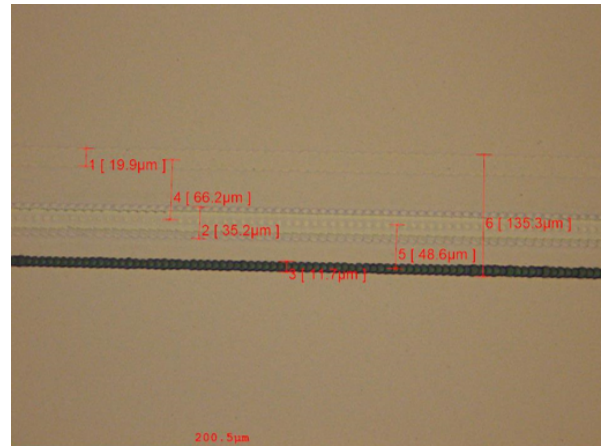


Figure 5.30: The scribe design after laser parameter optimization

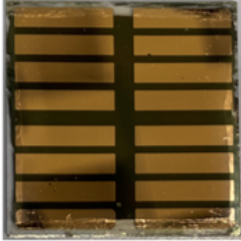
The inactive area losses are a significant study in this thesis. Initially, the P1-P3 width was around  $280 \mu\text{m}$  before laser parameter optimization. The new P1 parameter helps perform a continuous scribe which isolates the front electrode. The width of the P1 scribe was reduced from  $24\text{-}25 \mu\text{m}$  to  $19\text{-}20 \mu\text{m}$ , and the performed scribe has no cracks on the edges and underneath layers. Secondly, the P2 scribe is the most vital one for quality interconnection. The goal has been achieved by reducing the P2 width from  $110\text{-}115 \mu\text{m}$  to  $30\text{-}35 \mu\text{m}$ . The width reduction does not compromise the module performance.



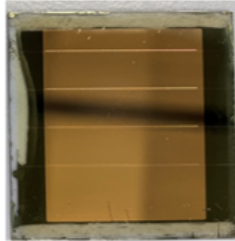
The module performance in figure 5.21 concurs with the above statement. Finally, the optimized P3 scribe laser parameter has a slight reduction in width, but it solved the central issue with the insulation of the back electrode. The final P1-P3 width was reduced from  $280 \mu\text{m}$  to  $135 \mu\text{m}$ . It helped increase the GFF from 94.3% to 97.3%. Further, the effects on module performance and interconnection losses are analyzed.

Parameter	Values	Parameter	Values
Voc (V)	1.05	Voc/cell (V)	1.0375
Jsc(mA/cm <sup>2</sup> )	21.48	Jsc <sub>active</sub> (mA/cm <sup>2</sup> )	20.10
FF (%)	78.25	FF (%)	75.55
Eff (%)	17.14	Eff <sub>active</sub> (%)	16.20

Figure 5.31: Performance data of cell (left) and module (right) before laser parameter optimization



Parameter	Values
Voc (V)	1.05
Jsc(mA/cm <sup>2</sup> )	20.33
FF (%)	78.08
Eff (%)	16.70



Parameter	Values
Voc/cell (V)	1.0375
Jsc <sub>active</sub> (mA/cm <sup>2</sup> )	19.62
FF (%)	77
Eff <sub>active</sub> (%)	15.72

Figure 5.32: Performance data of cell (left) and module (right) after laser parameter optimization

The efficiency of the up-scaling performed is analyzed with the help of a reference cell. In the above figure 5.32, the processed cell and module, along with their electrical performance, are shown to analyze the drop in electrical performance from a cell to a module to exhibit the scope of improvements in future upscaling. From the measured data, the reduction in short circuit density from cell to module, is relatively due to inactive area losses, which after optimization is 3%. Moreover, when upscaled, the drop in fill factor is entirely due to the interconnection quality at the junctions. The decline of 1% FF from cell to the module is the interconnection loss across the module, showing the possibility for P2 scribe improvement.

The decrease in the percentage of module performance before and after optimization is shown in the below table 5.5. Finally, the new set of laser parameters can be used to process the next batch of modules, as the performance loss from cell to module is 1%.

Before optimization	Relative drop in performance (%)	After optimization	Relative drop in performance (%)
Voc	1.1	Voc	1.1
Jsc	6.4	Jsc	3.4
FF	3.4	FF	1.3
Eff	5.4	Eff	5.8

Table 5.5: Relative drop in performance after upscaling

# Chapter 6

## Conclusion and Outlook

### 6.1 Conclusion

The goal of the thesis has been achieved by retaining the electrical performance of inverted perovskite-based solar cells when up-scaled, with minimal losses. The performed P1 scribe with IR laser successfully isolates the front electrode and does not damage the glass underneath for the power of 260 MCS and 300 mm/s. Moreover, the width of the P1 scribe was reduced to 19  $\mu\text{m}$  to minimize the inactive area losses. Furthermore, a quality and efficient P2 interconnection was obtained for inverted PSC with a ps UV laser. The complete ablation of  $\text{NiO}_x$  was achieved with a laser fluence of 440  $\text{mJ}/\text{cm}^2$ , power of 290 MCS, and scribe speed of 200 mm/s. This work shows that at the expense of ablating a part of ITO at the scribe spot, there is a scope for obtaining an efficient P2 interconnection by completely removing  $\text{NiO}_x$ .

The qualitative analysis performed using SEM in EDS mode showed that, at a fluence 440  $\text{mJ}/\text{cm}^2$  there is a complete removal of  $\text{NiO}_x$  as compared to ablation at threshold fluence 110  $\text{mJ}/\text{cm}^2$ . The quantitative analysis of the P2 scribe helped assess the line contact quality by measuring the contact resistance. The optimal contact length of 30  $\mu\text{m}$  for a fluence of 440  $\text{mJ}/\text{cm}^2$  was found from transfer length measurements using TLM analysis. The set of optimized parameters was used to make the P2 scribe. In addition, the P3 scribe at power 270 MCS and scribe speed 200mm/s performs a continuous scribe line without any incomplete removal of copper, and the width of the scribe was measured to be around 11  $\mu\text{m}$ . It further minimizes the inactive area losses and completes the module's fabrication.

In conclusion, after P1-P2-P3 scribe laser parameter optimization, the inactive area loss was successfully reduced by increasing the GFF by 3%, and the interconnection loss was down to 1% when up-scaled from cell to module. It shows the increase in optical gain percentage and reduction in electrical loss percentage of the upscaled module before and after optimization of laser parameters.

## 6.2 Outlook

The different parameters involved with the laser scribing process make it a more complex procedure as each parameter has a different effect on the performed scribe. Currently, the P1 scribe is performed using an IR laser; it was decided based on an absorptance spectrum plot. However, certain researches show the advantage of using UV and green laser [55]. The possibility of using other wavelengths can be explored in the future for P1-P2-P3 scribes. It could further help to reduce the inactive area losses and thermal stress at adjacent layers. Another parameter to be studied is the raster scanning distance. Further reduction of RSD can increase the GFF and reduce the contact resistance at scribe lines by forming continuous parallel scribes without an  $NiO_x$  left behind between two parallel P2 scribes. It could pave the way for an even smaller P2 width and reduce interconnection loss.

From the current P1-P2-P3 scribe design, the distance between the edges of P1-P3 can be reduced by bringing P1 and P2 closer to each other; this could increase the GFF. To conclude, a study can be done based on the observations of P2 scribes at lower contact lengths although current crowding is one parameter affecting module performance at smaller contact length. A further detailed study could be undertaken to understand the reason behind the drop in module performance, although the contact resistance at those scribes is considerably lower.

## references

- [1] Sankey. “IEA”. In: Energy balance, International Energy Agency (2019).
- [2] EPA- Environmental Protection Agency. “Greenhouse-gases”. In: Climate change indicators (2022).
- [3] International Energy Agency. Review 2021 Assessing the effects of economic recoveries on global energy demand and CO 2 emissions in 2021 Global Energy. Tech. rep. 2021. URL: [www.iea.org/t&c/](http://www.iea.org/t&c/).
- [4] C2ES. “Renewable Energy Center for Climate and Energy Solutions”. In: Renewable energy (2020).
- [5] Frankfurt school. “GTR2019”. In: GLOBAL TRENDS IN RENEWABLE ENERGY INVESTMENT (2019).
- [6] Fraunhofer Ise and Pse Projects GmbH. Photovoltaics Report. Tech. rep. 2022. URL: [www.ise.fraunhofer.de](http://www.ise.fraunhofer.de).
- [7] NREL. “best-research-cell-efficiencies-rev220126”. In: Cell Efficiency (2022).
- [8] F. Meillaud et al. Recent advances and remaining challenges in thin-film silicon photovoltaic technology. Sept. 2015. DOI: 10.1016/j.mattod.2015.03.002.
- [9] EMILIANO BELLINI. “CSEM, EPFL achieve 31.25% efficiency for tandem perovskite-silicon solar cell”. In: (July 2022).
- [10] Henry J. Snaith et al. “Charge generation and photovoltaic operation of solid-state dye-sensitized solar cells incorporating a high extinction coefficient indolene-based sensitizer”. In: Advanced Functional Materials 19.11 (June 2009), pp. 1810–1818. ISSN: 1616301X. DOI: 10.1002/adfm.200801751.
- [11] Ajay Kumar Jena, Ashish Kulkarni, and Tsutomu Miyasaka. “Halide Perovskite Photovoltaics: Background, Status, and Future Prospects”. In: Chemical Reviews 119.5 (Mar. 2019), pp. 3036–3103. ISSN: 15206890. DOI: 10.1021/acs.chemrev.8b00539.
- [12] Martin A. Green, Anita Ho-Baillie, and Henry J. Snaith. The emergence of perovskite solar cells. 2014. DOI: 10.1038/nphoton.2014.134.
- [13] Terry Chien Jen Yang et al. High-Bandgap Perovskite Materials for Multijunction Solar Cells. Aug. 2018. DOI: 10.1016/j.joule.2018.05.008.
- [14] Mohammed Istafaul Haque Ansari, Ahsanulhaq Qurashi, and Mohammad Khaja Nazeeruddin. Frontiers, opportunities, and challenges in perovskite solar cells: A critical review. June 2018. DOI: 10.1016/j.jphotochemrev.2017.11.002.

- [15] Wan Jian Yin, Tingting Shi, and Yanfa Yan. “Unique properties of halide perovskites as possible origins of the superior solar cell performance”. In: *Advanced Materials* 26.27 (July 2014), pp. 4653–4658. ISSN: 15214095. DOI: 10.1002/adma.201306281.
- [16] Qi Chen et al. Under the spotlight: The organic-inorganic hybrid halide perovskite for optoelectronic applications. July 2015. DOI: 10.1016/j.nantod.2015.04.009.
- [17] Samrana Kazim et al. “Perovskite as light harvester: A game changer in photovoltaics”. In: *Angewandte Chemie - International Edition* 53.11 (Mar. 2014), pp. 2812–2824. ISSN: 14337851. DOI: 10.1002/anie.201308719.
- [18] Henry J. Snaith. Perovskites: The emergence of a new era for low-cost, high-efficiency solar cells. Nov. 2013. DOI: 10.1021/jz4020162.
- [19] P. Ghosh et al. “Influence of Nanostructures in Perovskite Solar Cells”. In: *Reference Module in Materials Science and Materials Engineering*. Elsevier, 2016. DOI: 10.1016/b978-0-12-803581-8.04062-5.
- [20] Jin Wook Lee et al. “Formamidinium and cesium hybridization for photo- and moisture-stable perovskite solar cell”. In: *Advanced Energy Materials* 5.20 (Oct. 2015). ISSN: 16146840. DOI: 10.1002/aenm.201501310.
- [21] Xiao Xin Gao et al. “Stable and High-Efficiency Methylammonium-Free Perovskite Solar Cells”. In: *Advanced Materials* 32.9 (Mar. 2020). ISSN: 15214095. DOI: 10.1002/adma.201905502.
- [22] Zhen Li and Kai Zhu. “Ultra-High Efficiency Perovskite-Perovskite Tandem Solar Cells”. In: *Chemistry and Nanoscience Center, National Renewable Energy Laboratory* (2018).
- [23] Yang Zhou et al. “Distribution of bromine in mixed iodide-bromide organolead perovskites and its impact on photovoltaic performance”. In: *Journal of Materials Chemistry A* 4.41 (2016), pp. 16191–16197. ISSN: 20507496. DOI: 10.1039/c6ta07647e.
- [24] Lei Meng et al. “Recent Advances in the Inverted Planar Structure of Perovskite Solar Cells”. In: *Accounts of Chemical Research* 49.1 (Jan. 2016), pp. 155–165. ISSN: 15204898. DOI: 10.1021/acs.accounts.5b00404.
- [25] Luísa Andrade Joana Príncipe Vera C. M. Duarte. “Inverted Perovskite Solar Cells: The Emergence of a Highly Stable and Efficient Architecture”. In: *Energy Technology* 10.4 (Dec. 2021).
- [26] Tanghao Liu et al. “Inverted Perovskite Solar Cells: Progresses and Perspectives”. In: *Advanced Energy Materials* 6.17 (Sept. 2016). ISSN: 16146840. DOI: 10.1002/aenm.201600457.
- [27] Qi Jiang et al. “Planar-Structure Perovskite Solar Cells with Efficiency beyond 21%”. In: *Advanced Materials* 29.46 (Dec. 2017). ISSN: 15214095. DOI: 10.1002/adma.201703852.
- [28] IEEE Staff. Thermal and Environmental Stability of Semi-Transparent Perovskite Solar Cells for Tandems by a Solution-Processed Nanoparticle Buffer Layer and Sputtered ITO Electrode. IEEE, 2016. ISBN: 9781509027248.

- [29] Jae Ho Kim et al. “Flexible ITO films with atomically flat surfaces for high performance flexible perovskite solar cells”. In: *Nanoscale* 10.44 (Nov. 2018), pp. 20587–20598. ISSN: 20403372. DOI: 10.1039/c8nr06586a.
- [30] F. Behrouznejad et al. “A study on utilizing different metals as the back contact of CH<sub>3</sub>NH<sub>3</sub>PbI<sub>3</sub> perovskite solar cells”. In: *Journal of Materials Chemistry A* 4.35 (2016), pp. 13488–13498. ISSN: 20507496. DOI: 10.1039/c6ta05938d.
- [31] Michael Serhan et al. “Degradation observations of encapsulated planar CH<sub>3</sub>NH<sub>3</sub>PbI<sub>3</sub> perovskite solar cells at high temperatures and humidity”. In: *AIChE Annual Meeting, Conference Proceedings*. Vol. 2019-November. American Institute of Chemical Engineers, 2019. ISBN: 9780816911127. DOI: 10.1039/x0xx00000x.
- [32] Zezhu Jin et al. “Modification of NiO: X hole transport layer for acceleration of charge extraction in inverted perovskite solar cells”. In: *RSC Advances* 10.21 (Mar. 2020), pp. 12289–12296. ISSN: 20462069. DOI: 10.1039/d0ra00209g.
- [33] Tanghao Liu et al. “Inverted Perovskite Solar Cells: Progresses and Perspectives”. In: *Advanced Energy Materials* 6.17 (Sept. 2016). ISSN: 16146840. DOI: 10.1002/aenm.201600457.
- [34] Chuanliang Chen et al. “Effect of BCP buffer layer on eliminating charge accumulation for high performance of inverted perovskite solar cells”. In: *RSC Advances* 7.57 (2017), pp. 35819–35826. ISSN: 20462069. DOI: 10.1039/c7ra06365b.
- [35] Jingjing Zhao et al. “Is Cu a stable electrode material in hybrid perovskite solar cells for a 30-year lifetime?” In: *Energy and Environmental Science* 9.12 (Dec. 2016), pp. 3650–3656. ISSN: 17545706. DOI: 10.1039/c6ee02980a.
- [36] Zheng Chen et al. *Processing and Preparation Method for High-Quality Opto-Electronic Perovskite Film*. Oct. 2021. DOI: 10.3389/fmats.2021.723169.
- [37] Matt Hughes. “What is DC Sputtering”. In: *Semicore Equipment* (Nov. 2016).
- [38] D. Depla, S. Mahieu, and J. E. Greene. “Sputter Deposition Processes”. In: *Handbook of Deposition Technologies for Films and Coatings*. Elsevier Inc., 2010, pp. 253–296. ISBN: 9780815520313. DOI: 10.1016/B978-0-8155-2031-3.00005-3.
- [39] Florence Archet. “Thin Film Processing Method”. In: *Dracula technologies* (). URL: <https://dracula-technologies.com/thin-film-processing-method-1/>.
- [40] Ruth Cherrington and Jianwang Liang. “Materials and Deposition Processes for Multifunctionality”. In: *Design and Manufacture of Plastic Components for Multifunctionality: Structural Composites, Injection Molding, and 3D Printing*. Elsevier Inc., 2016, pp. 19–51. ISBN: 9780323353847. DOI: 10.1016/B978-0-323-34061-8.00002-8.
- [41] Norm Hardy. “Thin film deposition by thermal evaporation”. In: *semicore equipment* (Sept. 2013).
- [42] Francesco Di Giacomo et al. “Upscaling inverted perovskite solar cells: Optimization of laser scribing for highly efficient mini-modules”. In: *Micromachines* 11.12 (Dec. 2020), pp. 1–13. ISSN: 2072666X. DOI: 10.3390/mi11121127.
- [43] Oxonian Park. *MSV700 Operators Manual System Model MSV700 Serial number: 125*. Tech. rep.

- 
- [44] Dieter Bäuerle. *Laser Processing and Chemistry*. 4th ed. 2011, pp. 279–313.
- [45] Georg Schnell, Ulrike Duenow, and Hermann Seitz. “Effect of laser pulse overlap and scanning line overlap on femtosecond laser-structured Ti6Al4V surfaces”. In: *Materials* 13.4 (Feb. 2020). ISSN: 19961944. DOI: 10.3390/ma13040969.
- [46] Xuesong Lin et al. Efficiency progress of inverted perovskite solar cells. Nov. 2020. DOI: 10.1039/d0ee02017f.
- [47] Aslihan Babayigit et al. Gas Quenching for Perovskite Thin Film Deposition. July 2018. DOI: 10.1016/j.joule.2018.06.009.
- [48] Bugra Turan et al. “Cost-Effective Absorber Patterning of Perovskite Solar Cells by Nanosecond Laser Processing”. In: *Solar RRL* 1.2 (Feb. 2017). ISSN: 2367198X. DOI: 10.1002/solr.201700003.
- [49] H F Castillo González. Development of a semi transparent perovskite module Optimization of the laser scribes for the interconnection. Tech. rep. URL: [http://repository.tudelft.nl/.](http://repository.tudelft.nl/)
- [50] R. Geremia, D. Karnakis, and D. P. Hand. “The role of laser pulse overlap in ultra-fast thin film structuring applications”. In: *Applied Physics A: Materials Science and Processing* 124.9 (Sept. 2018). ISSN: 14320630. DOI: 10.1007/s00339-018-2045-z.
- [51] Bugra Turan and Stefan Haas. “Scribe width optimization of absorber laser ablation for thin-film silicon solar modules”. In: *Journal of Laser Micro Nanoengineering* 8.3 (Dec. 2013), pp. 234–243. ISSN: 18800688. DOI: 10.2961/jlmn.2013.03.0009.
- [52] Lucija Rakocevic. Upscaling Perovskite Based Thin-Film Photovoltaic Modules for Customized Applications. Tech. rep.
- [53] Contact resistance and TLM measurements. Tech. rep.
- [54] Sidhant Grover. Effect of Transmission Line Measurement (TLM) Geometry on Effect of Transmission Line Measurement (TLM) Geometry on Specific Contact Resistivity Determination Specific Contact Resistivity Determination. Tech. rep. 2016. URL: <https://scholarworks.rit.edu/theses>.
- [55] Laser Patterning of ITO for Flat Panel Displays. Tech. rep. 2011. URL: [www.newport.com/spectra-physics](http://www.newport.com/spectra-physics).



# Appendix A

## Appendix 1

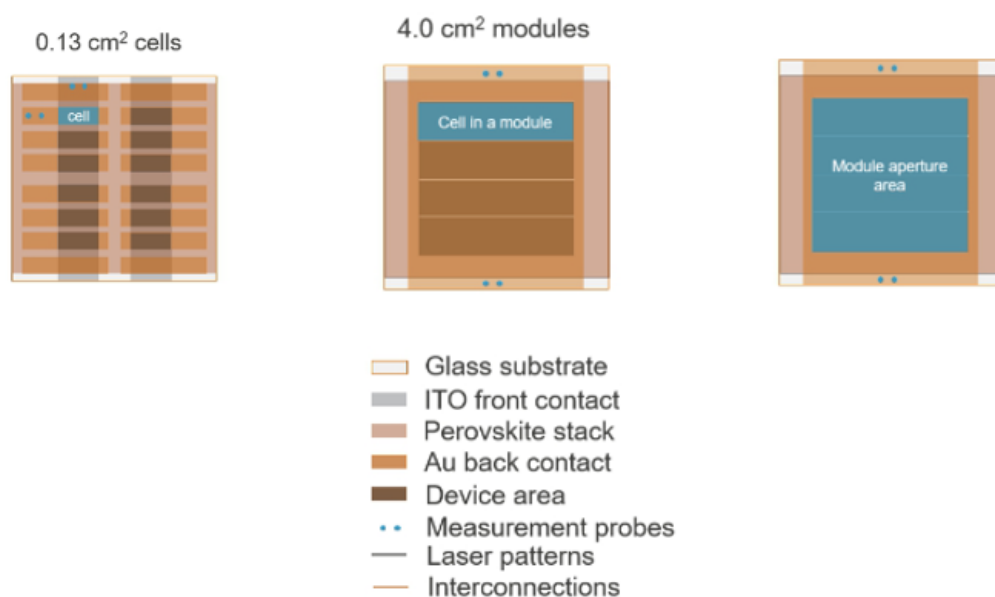


Figure A.1: Design of single cell and mini-module used in the thesis [52]

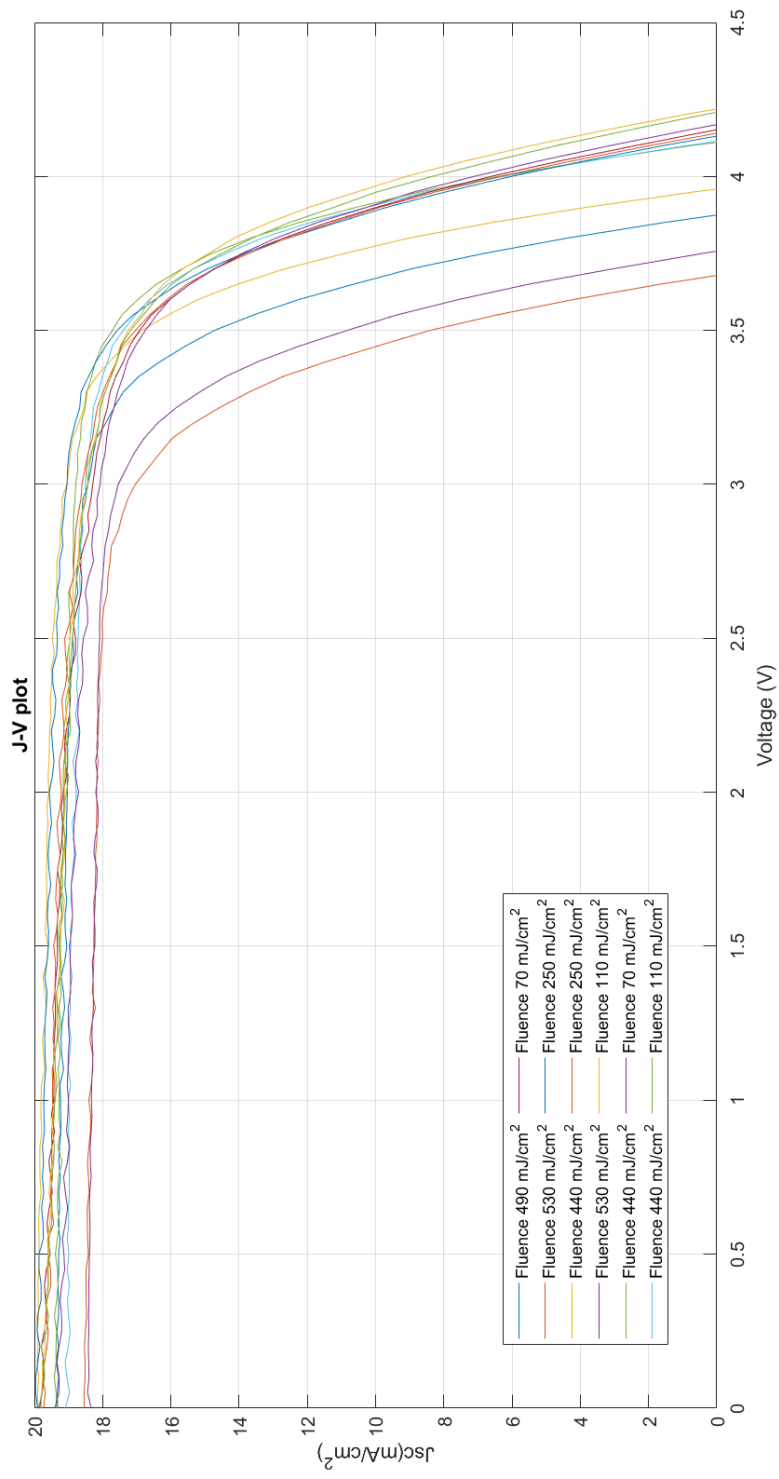


Figure A.2: J-V plot of modules in figure 5.13

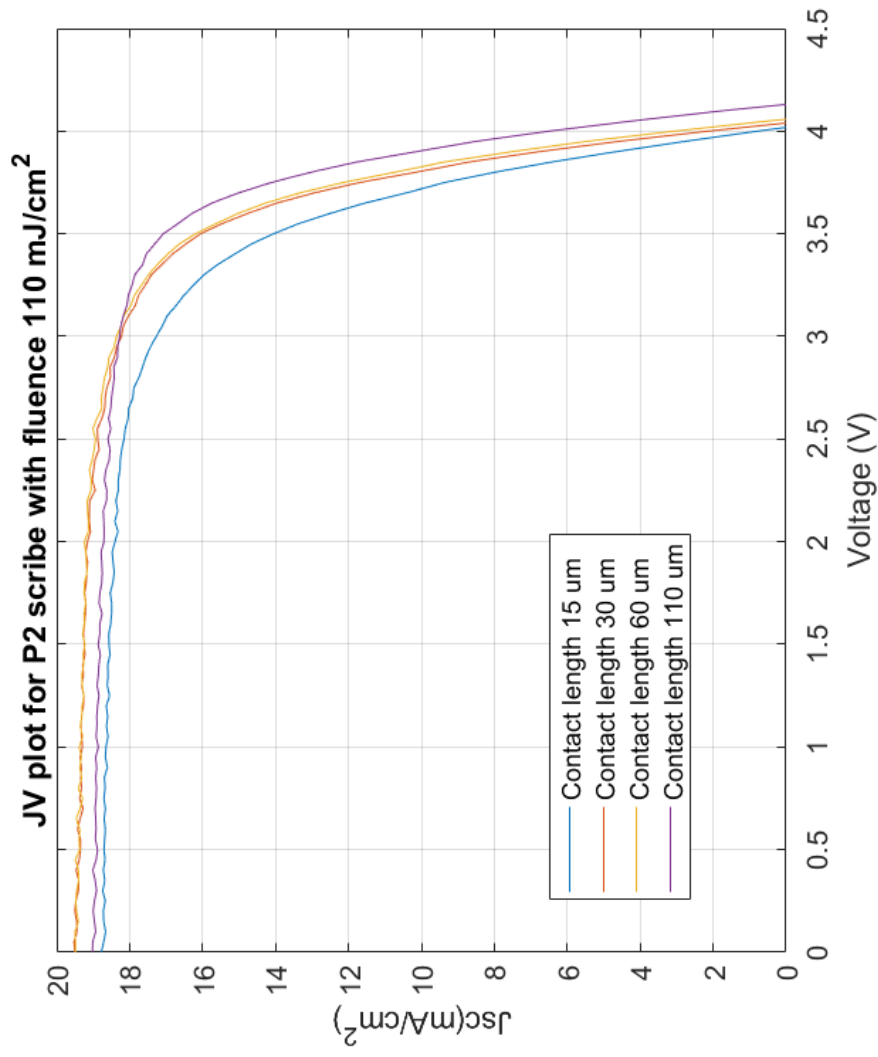


Figure A.3: JV plot of modules with P2 scribe fluence 110mJ/cm<sup>2</sup> and at different contact length

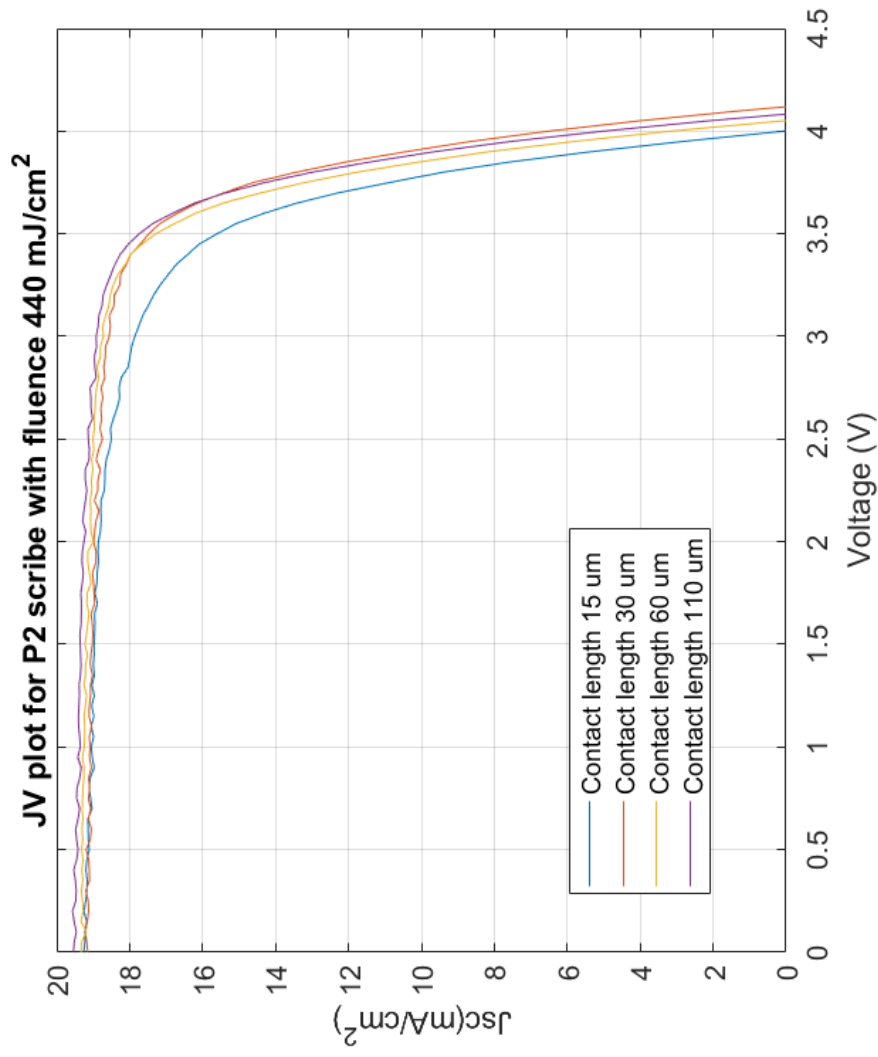


Figure A.4: JV plot of modules with P2 scribe fluence 440mJ/cm<sup>2</sup> and at different contact length

Fluence mJ/cm <sup>2</sup>	P2 width um	Contact resistance ohm	Sheet resistance ohm/sq	Transfer length um	Resistivity ohm/cm <sup>2</sup>
110	15	0,1255	19,1725	32,84261	0,000207
	20	0,15087	19,1684	39,35383	0,000297
	30	0,2523	14,40145	87,59708	0,001105
	80	0,1729	14,13015	61,03969	0,000526
	110	0,11211	13,52715	41,40481	0,000232
	250	0,03175	17,2	9,229651	1,47E-05
250	15	0,09385	18,8847	24,85345	0,000117
	20	0,10416	19,19215	27,13609	0,000141
	30	0,126245	14,60795	43,21106	0,000273
	80	0,113885	13,765	41,35874	0,000235
	110	0,093115	13,61225	34,20265	0,000159
	250	0,0322	17,45	9,212318	1,48E-05
440	15	0,098	19,37225	25,30037	0,000124
	20	0,1534	19,26805	39,83148	0,000306
	30	0,13949	13,39525	52,06696	0,000363
	80	0,06686	14,265	23,43293	7,83E-05
	110	0,055525	13,73095	20,21892	5,61E-05
	250	0,03689	17,66075	10,44406	1,93E-05
490	30	0,06375	13,67855	23,30291	7,43E-05
	80	0,068655	13,2157	25,97479	8,92E-05
	110	0,05481	13,39105	20,46516	5,61E-05
530	30	0,106755	13,7609	38,78925	0,000207
	80	0,06968	13,75765	25,32409	8,82E-05
	110	0,051605	13,671	18,87389	4,87E-05

Table A.1: TLM measurements at different fluence and Contact length